11

Frequency-Domain Differential Equation Formulations for Open Three-Dimensional Problems

In the two-dimensional formulations considered in Chapters 2 and 3, differential equations are shown to offer computational advantages over volume integral equations because of the sparsity of the resulting matrix. Similar advantages arise in three dimensions. In this chapter, the three-dimensional vector Helmholtz equation is used as the basis for several open-region formulations. Radiation boundary conditions are developed for spherical and nonspherical boundary shapes. Discretizations are obtained using mixed-order curl-conforming basis functions, whose properties have been previously explored in Chapter 9. A formulation for general axisymmetric scatterers is developed. Finally, an alternative approach incorporating traditional node-based Lagrangian basis functions is reviewed. While there has been much progress in this field during recent years, three-dimensional differential equation implementations are far from mature, and their performance has not been evaluated as extensively as the methods described in previous chapters.

11.1 WEAK VECTOR HELMHOLTZ EQUATION AND BOUNDARY CONDITIONS

Three-dimensional time-harmonic electromagnetic fields can be expressed in terms of Maxwell's equations, the vector Helmholtz equations, or several different formulations involving scalar and vector potential functions. Although numerical approaches can be developed for any of these equations, this chapter emphasizes schemes involving the curl–curl form of the vector Helmholtz equations. These equations involve only one type of

unknown field, $\bar{E}$ or $\bar{H}$, and are similar in appearance to the scalar Helmholtz equations used in previous chapters. In a source-free isotropic region, the vector Helmholtz equations are

$$\nabla \times \left(\frac{1}{\mu_r}\nabla \times \bar{E}\right) = k^2 \varepsilon_r \bar{E} \tag{11.1}$$

$$\nabla \times \left(\frac{1}{\varepsilon_r}\nabla \times \bar{H}\right) = k^2 \mu_r \bar{H} \tag{11.2}$$

These equations are obtained from Maxwell's curl equations (1.1) and (1.2) and sometimes admit solutions that fail to satisfy Gauss' laws in (1.3) and (1.4). This issue is explored in Chapter 9, where it is shown that the eigenfunctions of the curl–curl operator fall into two families, one of which has zero curl and cannot represent source-free electromagnetic fields (the "nullspace" family). The other eigenfunction family represents true solutions of Maxwell's equations. Although both eigenfunction families may be present in the discrete matrix operator arising from a numerical discretization, the nullspace eigenfunctions can be separated from the true solutions through the use of special curl-conforming basis functions developed in Chapter 9. Consequently, we use these basis functions throughout this chapter.

The vector Helmholtz equation (11.1) can be converted into a weak form by constructing a dot product with a vector testing function $\bar{T}$ and using the vector identity

$$\bar{T} \cdot \nabla \times \bar{A} = \nabla \times \bar{T} \cdot \bar{A} - \nabla \cdot (\bar{T} \times \bar{A}) \tag{11.3}$$

the divergence theorem

$$\iiint_{\Gamma} \nabla \cdot (\bar{T} \times \bar{A})\, dv = \iint_{\partial\Gamma} (\bar{T} \times \bar{A}) \cdot \hat{n}\, dS \tag{11.4}$$

and the vector identity

$$(\bar{T} \times \bar{A}) \cdot \hat{n} = -\bar{T} \cdot (\hat{n} \times \bar{A}) \tag{11.5}$$

to produce

$$\iiint_{\Gamma} \frac{1}{\mu_r}\nabla \times \bar{T} \cdot \nabla \times \bar{E} - k^2 \varepsilon_r \bar{T} \cdot \bar{E} = -\iint_{\partial\Gamma} \frac{1}{\mu_r}\bar{T} \cdot \hat{n} \times (\nabla \times \bar{E}) \tag{11.6}$$

$$\iiint_{\Gamma} \frac{1}{\varepsilon_r}\nabla \times \bar{T} \cdot \nabla \times \bar{H} - k^2 \mu_r \bar{T} \cdot \bar{H} = -\iint_{\partial\Gamma} \frac{1}{\varepsilon_r}\bar{T} \cdot \hat{n} \times (\nabla \times \bar{H}) \tag{11.7}$$

where Γ denotes the region of interest, $\partial\Gamma$ denotes the boundary of that region, and $\hat{n}$ is the outward normal vector along the boundary. As in the two-dimensional case, the weak equation relaxes the differentiability requirements imposed on the field representation. In deriving (11.6) and (11.7), we have assumed the boundedness of the curl operations $\nabla \times \bar{T}$, $\nabla \times \bar{E}$, and $\nabla \times \bar{H}$. These derivatives are bounded if the field representation maintains tangential continuity throughout the computational domain. If the basis functions ultimately used for these quantities do not ensure tangential continuity between cells, Dirac delta functions occur along the interfaces and must be included in (11.6) and (11.7). [Equivalently, additional boundary integrals similar in form to the right-hand sides of (11.6) and (11.7) must be included along the cell interfaces.]

The boundary integrals on the right-hand side of (11.6) and (11.7) provide the means for incorporating boundary conditions. If $\partial\Gamma$ is a perfect electric conductor, the boundary condition

$$\hat{n} \times \bar{E} = 0 \tag{11.8}$$

can be used with the weak equation (11.6). The imposition of (11.8) requires that the field representation used for $\bar{E}$ satisfy (11.8) along $\partial\Gamma$ in the strong sense (exactly). In essence, this is equivalent to the Dirichlet type of boundary condition used in the scalar case. It is also known as an *essential* boundary condition since it must be imposed in order to be satisfied in the limit of an infinite number of unknowns. Since the tangential component of the field representation is specified along $\partial\Gamma$, there will be no need for testing functions with a nonzero tangential component along $\partial\Gamma$. In other words, the testing functions used to construct the system of equations should also satisfy (11.8). It follows that the boundary integral in (11.6) does not contribute to the system of equations and can be ignored.

The boundary condition

$$\hat{n} \times (\nabla \times \bar{H}) = 0 \tag{11.9}$$

also describes a perfect electric conductor and is applicable to the weak equation (11.7). The imposition of (11.9) is accomplished by discarding the boundary integral on the right-hand side of (11.7). This condition is similar in form to the Neumann type of boundary condition used in the scalar case and is also known as a *natural* boundary condition since it does not have to be exactly satisfied by the field representation in order to be realized in the limiting case (an infinite number of unknowns). By carving a region out of the mesh and using the same field representation within the surrounding cells as is used throughout the interior volume (in other words, doing nothing special at the boundary), (11.9) will be automatically imposed and the procedure will treat the region as a perfect electric conductor.

Scattering problems are usually posed in the context of an RBC on $\partial\Gamma$. In practice, the RBC is of the form

$$\hat{n} \times (\nabla \times \bar{E}^s) = L(\bar{E}^s) \tag{11.10}$$

or

$$\hat{n} \times (\nabla \times \bar{H}^s) = L(\bar{H}^s) \tag{11.11}$$

where L is some linear operator. These expressions are substituted directly into the boundary integrals appearing on the right-hand side of the weak equations, after which the scattered field may be combined with the incident field to leave the undetermined quantities entirely in terms of the total field. As in the two-dimensional case discussed in Chapter 3, exact RBCs are global in nature and couple the field around the entire boundary. Thus, they create fill-in within the global matrix equation. For improved numerical efficiency, approximate local RBCs have been developed that preserve the matrix sparsity. Several different RBCs will be discussed in the following sections.

11.2 DISCRETIZATION USING CT/LN AND LT/QN FUNCTIONS FOR THREE-DIMENSIONAL CAVITIES [1]

To illustrate the discretization procedure, we initially consider the numerical solution of the weak equation in (11.6) or (11.7) for closed cavities bounded by perfect electric walls. We will also use this example to illustrate the relative accuracy of the CT/LN and LT/QN functions defined in Table 9.12 for tetrahedral cells. These basis functions belong to Nedelec's curl-conforming spaces [2], and they provide tangential continuity between cells and ensure that the nullspace eigenfunctions are separated from the true physical solutions.

Consider a closed cavity bounded by perfect electric walls. Equation (11.6) can be written in the form of an eigenvalue equation for the resonant wavenumber

$$\iiint_\Gamma \frac{1}{\mu_r} \nabla \times \bar{T} \cdot \nabla \times \bar{E} = k^2 \iiint_\Gamma \varepsilon_r \bar{T} \cdot \bar{E} \tag{11.12}$$

where the boundary integral has been dropped since it does not contribute for p.e.c. walls as long as (11.8) is imposed on the expansion functions used for $\bar{E}$. The cavity interior can be discretized into tetrahedral cells, and the electric field represented by vector basis functions

$$\bar{E}(x, y, z) \cong \sum_{n=1}^{N} e_n \bar{B}_n(x, y, z) \tag{11.13}$$

Consider the CT/LN basis functions from Table 9.12, which can be written in the form

$$\bar{B}_n = w_n(L_i \nabla L_j - L_j \nabla L_i) \tag{11.14}$$

where (L_1, L_2, L_3, L_4) are simplex coordinates (Section 9.6) and w_n denotes the length of the cell edge n, which is located between nodes i and j. Each CT/LN function interpolates to the tangential component along an edge of the tetrahedral-cell mesh. If the CT/LN functions are also used for testing, and the cavity is homogeneous, an eigenvalue equation $\mathbf{Ae} = k^2\mathbf{Be}$ is obtained, where

$$A_{mn} = \iiint_\Gamma \nabla \times \bar{B}_m \cdot \nabla \times \bar{B}_n \, dx \, dy \, dz \tag{11.15}$$

$$B_{mn} = \iiint_\Gamma \bar{B}_m \cdot \bar{B}_n \, dx \, dy \, dz \tag{11.16}$$

As in the two-dimensional case, the global matrices can be constructed on a cell-by-cell basis using 6×6 element matrices that represent the evaluation of (11.15) and (11.16) over a single tetrahedron. Entries of the element matrices can be found using simplex coordinates, which for a given cell can be defined by the parameters (Section 9.6) associated with the transformation

$$L_i = \frac{1}{6V}(a_i + b_i x + c_i y + d_i z) \tag{11.17}$$

from Cartesian coordinates to simplex coordinates, where V denotes the cell volume. It follows that

$$\nabla L_i = \frac{1}{6V}(b_i \hat{x} + c_i \hat{y} + d_i \hat{z}) \tag{11.18}$$

For convenience, define

$$\bar{v}_{ij} = \nabla L_i \times \nabla L_j = \frac{\hat{x}(c_i d_j - d_i c_j) + \hat{y}(d_i b_j - b_i d_j) + \hat{z}(b_i c_j - c_i b_j)}{36V^2} \tag{11.19}$$

$$\Phi_{ij} = \nabla L_i \cdot \nabla L_j = \frac{b_i b_j + c_i c_j + d_i d_j}{36V^2} \tag{11.20}$$

These quantities are constant within a cell and can be determined from the coordinates of the four nodes that define the tetrahedron. Note that $\Phi_{ij} = \Phi_{ji}$ and $\bar{v}_{ij} = -\bar{v}_{ji}$.

The curl of a CT/LN basis function is given by

$$\nabla \times \bar{B}_n = w_n \nabla \times (L_i \nabla L_j - L_j \nabla L_i) = 2w_n \bar{v}_{ij} \tag{11.21}$$

Therefore, the element matrix entries for **A** in (11.15) are

$$A_{mn} = 4V w_m w_n \bar{v}_{pq} \cdot \bar{v}_{ij} \tag{11.22}$$

where p and q denote the node indices associated with edge m and i and j are the node indices for edge n. The element matrix entries for **B** can be obtained using

$$\begin{aligned} \bar{B}_m \cdot \bar{B}_n &= w_m w_n (L_p \nabla L_q - L_q \nabla L_p) \cdot (L_i \nabla L_j - L_j \nabla L_i) \\ &= w_m w_n (L_p L_i \Phi_{qj} - L_q L_i \Phi_{pj} - L_p L_j \Phi_{qi} + L_q L_j \Phi_{pi}) \end{aligned} \tag{11.23}$$

and have the form

$$B_{mn} = w_m w_n V (\Phi_{qj} M_{pi} - \Phi_{pj} M_{qi} - \Phi_{qi} M_{pj} + \Phi_{pi} M_{qj}) \tag{11.24}$$

where

$$M_{ij} = \frac{1}{V} \iiint_{\text{cell}} L_i L_j \, dv = \frac{1}{20} \begin{cases} 2 & i = j \\ 1 & \text{otherwise} \end{cases} \tag{11.25}$$

Equation (11.25) is evaluated using the integral formula [3]

$$\iiint (L_1)^i (L_2)^j (L_3)^k (L_4)^m \, dv = V \frac{3! i! j! k! m!}{(3 + i + j + k + m)!} \tag{11.26}$$

This completes the development of the element matrix entries for the CT/LN functions. As the global matrix is constructed in a cell-by-cell manner, entries that correspond to edges along the p.e.c. boundary are omitted to impose the essential boundary condition in (11.8). It is also necessary to ensure that the vector orientation of a CT/LN function is the same in all the cells bordering a common edge; a simple approach is to assign nodes i and j in (11.14) so that the vector always points from the smaller index to the larger.

Element matrix entries of order 20 can be constructed for LT/QN basis and testing functions from Table 9.12 in a similar manner. The development is complicated by the fact that there are two different types of LT/QN functions. There are two functions associated with each edge that can be expressed as

$$\bar{B}_n^{e1} = w_n L_i \nabla L_j \tag{11.27}$$

$$\bar{B}_n^{e2} = w_n L_j \nabla L_i \tag{11.28}$$

where i and j denote the node indices associated with edge n. There are also two functions associated with each face having the form

$$\bar{B}_n^{f1} = L_i L_j \nabla L_k - L_i L_k \nabla L_j \tag{11.29}$$

$$\bar{B}_n^{f2} = L_i L_j \nabla L_k - L_j L_k \nabla L_i \tag{11.30}$$

where i, j, k denote the indices of the nodes associated with face n. (The specific node-numbering scheme used in the construction to follow is depicted in Figure 11.1.)

From the numbering scheme in Figure 11.1 and the previous expressions, one can deduce that

$$\nabla \times \bar{B}_n^{e1} = w_n \nabla \times (L_i \nabla L_j) = w_n \bar{v}_{ij} \tag{11.31}$$

$$\nabla \times \bar{B}_n^{e2} = -w_n \bar{v}_{ij} \tag{11.32}$$

$$\nabla \times \bar{B}_n^{f1} = 2L_i \bar{v}_{jk} + L_j \bar{v}_{ik} - L_k \bar{v}_{ij} \tag{11.33}$$

$$\nabla \times \bar{B}_n^{f2} = L_i \bar{v}_{jk} + 2L_j \bar{v}_{ik} + L_k \bar{v}_{ij} \tag{11.34}$$

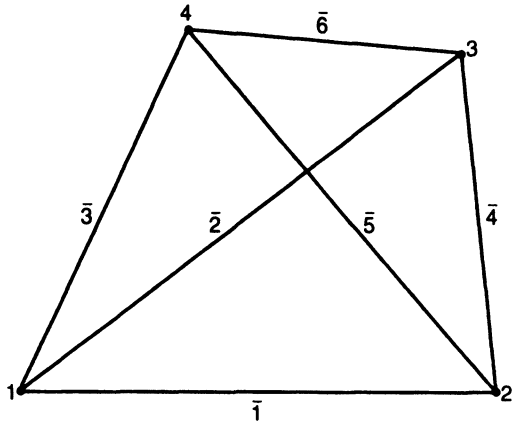

Local face, edge, and node conventions

Edge number	Node 1	Node 2	
1	1	2	
2	1	3	
3	1	4	
4	2	3	
5	2	4	
6	3	4	
Face number	**Node 1**	**Node 2**	**Node 3**
1	1	2	3
2	1	2	4
3	1	3	4
4	2	3	4

Figure 11.1 Node and edge indices for a tetrahedral cell. After [1]. ©1996 IEEE.

These relations are used to obtain the entries of the element matrix **A**, which are summarized in Table 11.1. Analogous expressions can be obtained for the entries of element matrix **B** using the quantities

$$N_{ijk} = \frac{1}{V} \iiint_{\text{cell}} L_i L_j L_k \, dv \tag{11.35}$$

$$P_{ijkm} = \frac{1}{V} \iiint_{\text{cell}} L_i L_j L_k L_m \, dv \tag{11.36}$$

obtained from (11.26). The entries of **B** are provided in Table 11.2.

To illustrate the performance of the tetrahedral-cell basis functions, when used with the electric field form of the vector Helmholtz equation, Table 11.3 shows the resonant frequencies of a three-dimensional cavity of dimension $1 \times 0.5 \times 0.75$ m. Results obtained using the CT/LN and the LT/QN basis functions for a tetrahedral-cell mesh with 300 cells, 120 nodes, 513 edges, and 694 faces are compared. The longest cell edge in the mesh was 0.274 m. This model produced a sparse matrix of order 231 for the CT/LN functions, containing 2835 nonzero entries, and order 1474 for the LT/QN functions, containing 49,124 nonzero entries. The results were obtained using a sparse-matrix eigenanalysis procedure similar to that proposed in [4]. From a number of similar examples, it has been observed

TABLE 11.1 Entries of Element Matrix **A** in (11.15) for LT/QN Basis and Testing Functions

$$A_{mn}^{e1e1} = A_{mn}^{e2e2} = -A_{mn}^{e1e2} = -A_{nm}^{e2e1} = Vw_m w_n \bar{v}_{pq} \cdot \bar{v}_{ij}$$

$$A_{mn}^{e1f1} = A_{nm}^{f1e1} = -A_{mn}^{e2f1} = -A_{nm}^{f1e2} = \frac{Vw_m}{4} \bar{v}_{pq} \cdot (2\bar{v}_{jk} + \bar{v}_{ik} - \bar{v}_{ij})$$

$$A_{mn}^{e1f2} = A_{nm}^{f2e1} = -A_{mn}^{e2f2} = -A_{nm}^{f2e2} = \frac{Vw_m}{4} \bar{v}_{pq} \cdot (2\bar{v}_{ik} + \bar{v}_{jk} + \bar{v}_{ij})$$

$$\begin{aligned} A_{mn}^{f1f1} = V(&4M_{pi}\bar{v}_{qr} \cdot \bar{v}_{jk} + 2M_{pj}\bar{v}_{qr} \cdot \bar{v}_{ik} - 2M_{pk}\bar{v}_{qr} \cdot \bar{v}_{ij} \\ &+ 2M_{qi}\bar{v}_{pr} \cdot \bar{v}_{jk} + M_{qj}\bar{v}_{pr} \cdot \bar{v}_{ik} - M_{qk}\bar{v}_{pr} \cdot \bar{v}_{ij} \\ &- 2M_{ri}\bar{v}_{pq} \cdot \bar{v}_{jk} - M_{rj}\bar{v}_{pq} \cdot \bar{v}_{ik} + M_{rk}\bar{v}_{pq} \cdot \bar{v}_{ij}) \end{aligned}$$

$$\begin{aligned} A_{mn}^{f1f2} = A_{nm}^{f2f1} = V(&2M_{pi}\bar{v}_{qr} \cdot \bar{v}_{jk} + 4M_{pj}\bar{v}_{qr} \cdot \bar{v}_{ik} + 2M_{pk}\bar{v}_{qr} \cdot \bar{v}_{ij} \\ &+ M_{qi}\bar{v}_{pr} \cdot \bar{v}_{jk} + 2M_{qj}\bar{v}_{pr} \cdot \bar{v}_{ik} + M_{qk}\bar{v}_{pr} \cdot \bar{v}_{ij} \\ &- M_{ri}\bar{v}_{pq} \cdot \bar{v}_{jk} - 2M_{rj}\bar{v}_{pq} \cdot \bar{v}_{ik} - M_{rk}\bar{v}_{pq} \cdot \bar{v}_{ij}) \end{aligned}$$

$$\begin{aligned} A_{mn}^{f2f2} = V(&M_{pi}\bar{v}_{qr} \cdot \bar{v}_{jk} + 2M_{pj}\bar{v}_{qr} \cdot \bar{v}_{ik} + M_{pk}\bar{v}_{qr} \cdot \bar{v}_{ij} \\ &+ 2M_{qi}\bar{v}_{pr} \cdot \bar{v}_{jk} + 4M_{qj}\bar{v}_{pr} \cdot \bar{v}_{ik} + 2M_{qk}\bar{v}_{pr} \cdot \bar{v}_{ij} \\ &+ M_{ri}\bar{v}_{pq} \cdot \bar{v}_{jk} + 2M_{rj}\bar{v}_{pq} \cdot \bar{v}_{ik} + M_{rk}\bar{v}_{pq} \cdot \bar{v}_{ij}) \end{aligned}$$

Note: **A** has the block structure

$$\mathbf{A} = \begin{bmatrix} A^{e1e1} & A^{e1e2} & A^{e1f1} & A^{e1f2} \\ A^{e2e1} & A^{e2e2} & A^{e2f1} & A^{e2f2} \\ A^{f1e1} & A^{f1e2} & A^{f1f1} & A^{f1f2} \\ A^{f2e1} & A^{f2e2} & A^{f2f1} & A^{f2f2} \end{bmatrix}$$

In the expressions in the table, p and q denote the node indices for edge m, while p, q, and r denote the node indices for face m. Similarly, i and j denote the node indices for edge n, while i, j, and k denote the three node indices associated with face n.

TABLE 11.2 Entries of Element Matrix **B** in (11.16) for LT/QN Basis and Testing Functions

$$B_{mn}^{e1e1} = Vw_m w_n \phi_{qj} M_{pi}$$

$$B_{mn}^{e1e2} = Vw_m w_n \phi_{qi} M_{pj}$$

$$B_{mn}^{e2e2} = Vw_m w_n \phi_{pi} M_{qj}$$

$$B_{mn}^{e1f1} = Vw_m (\phi_{qk} N_{pij} - \phi_{qj} N_{pik})$$

$$B_{mn}^{e2f1} = Vw_m (\phi_{pk} N_{qij} - \phi_{pj} N_{qik})$$

$$B_{mn}^{e1f2} = Vw_m (\phi_{qk} N_{pij} - \phi_{qi} N_{pjk})$$

$$B_{mn}^{e2f2} = Vw_m (\phi_{pk} N_{qij} - \phi_{pi} N_{qjk})$$

$$B_{mn}^{f1f1} = V(\phi_{rk} P_{pqij} - \phi_{rj} P_{pqik} - \phi_{qk} P_{prij} + \phi_{qj} P_{prik})$$

$$B_{mn}^{f1f2} = V(\phi_{rk} P_{pqij} - \phi_{ri} P_{pqjk} - \phi_{qk} P_{prij} + \phi_{qi} P_{prjk})$$

$$B_{mn}^{f2f2} = V(\phi_{rk} P_{pqij} - \phi_{ri} P_{pqjk} - \phi_{pk} P_{qrij} + \phi_{pi} P_{qrjk})$$

Note: **B** has the block structure of **A** in Table 11.1 and is symmetric across the main diagonal. Only entries for blocks above the main diagonal are shown.

TABLE 11.3 Lowest Nonzero Eigenvalues for Rectangular Brick-Shaped Cavity with $\varepsilon_r = 1$, $\mu_r = 1$, and dimensions 1.0 by 0.5 by 0.75 m

CT/LN	LT/QN	Exact
5.260	5.237	5.236 (TE_{101})
6.985	7.026	7.025 (TM_{110})
7.461	7.552	7.551 (TE_{011})
7.613	7.557	7.551 (TE_{201})
8.149	8.184	8.179 (TM_{111})
8.214	8.187	8.179 (TE_{111})
8.835	8.889	8.886 (TM_{210})

Note: The model consisted of 300 tetrahedral cells, with the longest cell edge 0.274 m. The discretization of the vector Helmholtz equation for the electric field required 231 unknowns with CT/LN basis functions and 1474 unknowns with LT/QN basis functions.

that the tetrahedral-cell CT/LN functions generally produce less than 15 nonzero entries per row of the **A** and **B** matrices, while the LT/QN functions typically produce about 35 nonzero entries per row (and can involve 70 or more).

To show accuracy trends, Figure 11.2 provides a comparison of the error in the resonant frequencies of the 1 × 0.5 × 0.75 m cavity. In this case, six different unstructured tetrahedral-cell meshes of various density were used. Figure 11.2 shows the average of the error in the first eight resonant frequencies versus the average edge length in each tetrahedral-cell mesh. The curve associated with the CT/LN functions has a slope near 2, while that associated with the LT/QN functions has a slope near 4. In this situation, the

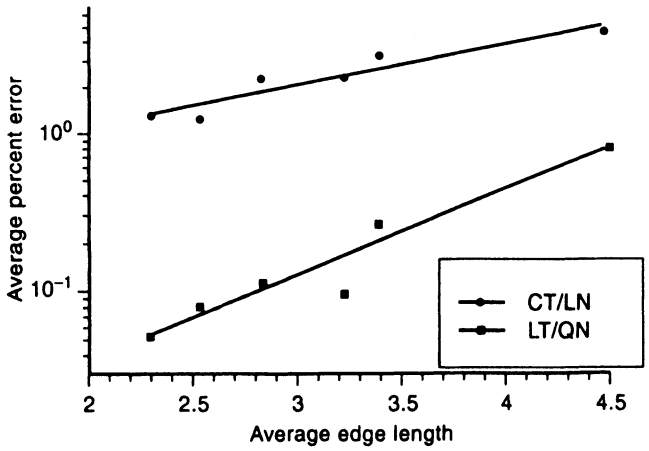

Figure 11.2 Comparison of the error produced by CT/LN and LT/QN discretizations as a function of the average edge length for the first eight nonzero resonant frequencies of a rectangular cavity. A curve fit through the actual data exhibits a slope of 1.98 for the CT/LN results and a slope of 3.86 for the LT/QN results. After [1]. ©1996 IEEE.

three-dimensional basis functions produce error behavior of $O(\Delta^2)$ for the CT/LN functions and $O(\Delta^4)$ for the LT/QN functions, similar to the two-dimensional functions investigated in Chapter 9.

11.3 EIGENFUNCTION RBC FOR SPHERICAL BOUNDARY SHAPES

An exact RBC can be obtained from an eigenfunction expansion of the scattered field. In the three-dimensional case, the scattered field at some point outside the scatterer can be expressed in the form

$$\bar{E}^s(r,\theta,\phi) = \sum_{n=1}^{\infty} \sum_{m=-n}^{n} A_{mn}\bar{M}_{mn} + B_{mn}\bar{N}_{mn} \tag{11.37}$$

where $\bar{M}_{mn}$ and $\bar{N}_{mn}$ are outward-propagating spherical vector wave functions defined as

$$\begin{aligned}\bar{M}_{mn} = &-\frac{jm}{r}\frac{P_n^m(\cos\theta)}{\sin\theta}\hat{H}_n^{(2)}(kr)e^{jm\phi}\hat{\theta} \\ &-\frac{1}{r}\sin\theta P_n^{m\prime}(\cos\theta)\hat{H}_n^{(2)}(kr)e^{jm\phi}\hat{\phi}\end{aligned} \tag{11.38}$$

$$\begin{aligned}\bar{N}_{mn} = &\frac{j}{r}\sin\theta P_n^{m\prime}(\cos\theta)\hat{H}_n^{(2)\prime}(kr)e^{jm\phi}\hat{\theta} \\ &+\frac{m}{r}\frac{P_n^m(\cos\theta)}{\sin\theta}\hat{H}_n^{(2)\prime}(kr)e^{jm\phi}\hat{\phi} \\ &+\frac{n(n+1)}{jkr^2}P_n^m(\cos\theta)\hat{H}_n^{(2)}(kr)e^{jm\phi}\hat{r}\end{aligned} \tag{11.39}$$

In these expressions, P_n^m denotes the associated Legendre polynomial and $\hat{H}_n^{(2)}$ denotes the alternative form of the spherical Hankel function of the second kind, as defined by Harrington [5]. (The vector wave functions differ slightly in form from those introduced by Stratton [6] and Ludwig [7] but provide an equivalent representation.) The $\bar{M}_{mn}$ and $\bar{N}_{mn}$ functions satisfy orthogonality relationships [7]

$$\int_{\phi=0}^{2\pi}\int_{\theta=0}^{\pi} \bar{M}_{mn} \times \bar{M}_{pq} \cdot \hat{r}\sin\theta\, d\theta\, d\phi = 0 \tag{11.40}$$

$$\int_{\phi=0}^{2\pi}\int_{\theta=0}^{\pi} \bar{N}_{mn} \times \bar{N}_{pq} \cdot \hat{r}\sin\theta\, d\theta\, d\phi = 0 \tag{11.41}$$

and

$$\int_{\phi=0}^{2\pi}\int_{\theta=0}^{\pi} \bar{M}_{mn} \times \bar{N}_{pq} \cdot \hat{r}\sin\theta\, d\theta\, d\phi = \begin{cases} 0 & q \neq n \text{ or } p \neq -m \\ \alpha_{mn}(r) & q = n \text{ and } p = -m \end{cases} \tag{11.42}$$

where

$$\alpha_{mn}(r) = -j\frac{\hat{H}_n^{(2)}(kr)\hat{H}_n^{(2)\prime}(kr)}{r^2}\frac{4\pi n(n+1)}{2n+1}\frac{(n+|m|)!}{(n-|m|)!} \tag{11.43}$$

Using (11.40)–(11.42), the coefficients in (11.37) can be determined to be

$$A_{mn} = \frac{1}{\alpha_{mn}(a)} \int_{\phi=0}^{2\pi} \int_{\theta=0}^{\pi} \bar{E}^s(a,\theta,\phi) \times \bar{N}_{(-m)n} \cdot \hat{r} \sin\theta \, d\theta \, d\phi \tag{11.44}$$

$$B_{mn} = \frac{1}{\alpha_{mn}(a)} \int_{\phi=0}^{2\pi} \int_{\theta=0}^{\pi} \bar{M}_{(-m)n} \times \bar{E}^s(a,\theta,\phi) \cdot \hat{r} \sin\theta \, d\theta \, d\phi \tag{11.45}$$

where a denotes the radius of a sphere enclosing the scatterer.

From (11.37) and with some manipulation, it is possible to show that

$$\hat{r} \times \nabla \times \bar{E}^s = jk \sum_{n=1}^{\infty} \sum_{m=-n}^{n} B_{mn} \hat{r} \times \bar{M}_{mn} - A_{mn} \hat{r} \times \bar{N}_{mn} \tag{11.46}$$

By substituting (11.44) and (11.45) into (11.46), we obtain

$$\begin{aligned} \hat{r} \times \nabla \times \bar{E}^s = jk \sum_{n=1}^{\infty} \sum_{m=-n}^{n} \frac{1}{\alpha_{mn}(a)} \\ \left(\hat{r} \times \bar{M}_{mn}(r,\theta,\phi) \int_{\phi'=0}^{2\pi} \int_{\theta'=0}^{\pi} \bar{M}_{(-m)n}(a,\theta',\phi') \times \bar{E}^s(a,\theta',\phi') \cdot \hat{r} \sin\theta' \, d\theta' \, d\phi' \right. \\ \left. - \hat{r} \times \bar{N}_{mn}(r,\theta,\phi) \int_{\phi'=0}^{2\pi} \int_{\theta'=0}^{\pi} \bar{E}^s(a,\theta',\phi') \times \bar{N}_{(-m)n}(a,\theta',\phi') \cdot \hat{r} \sin\theta' \, d\theta' \, d\phi' \right) \end{aligned} \tag{11.47}$$

This expression is an exact RBC that can be used to truncate the computational domain in a three-dimensional finite-element formulation. It is similar in form to the two-dimensional RBC developed in Section 3.3 and must be imposed on a spherical boundary surrounding the scatterer. By combining this expression with the incident electric field, (11.47) can be rewritten in terms of the total field and substituted into the boundary integral in (11.6) to complete the scattering formulation. A similar RBC has been derived in [8].

Although (11.47) is an exact condition, to the authors' knowledge, it has not been implemented in practice. There are several reasons for this, including the general complexity of the vector spherical wave functions. The exact RBC has the drawback that it must be imposed on a spherical boundary, which is generally undesirable since many additional unknowns are introduced by the process of padding a computational domain out to a sphere. Thus, the implementation of (11.47) may lead to an unacceptable increase in the order of the finite-element system. Furthermore, (11.47) couples the fields around the entire boundary, creating fill-in that increases the computational effort required to create and solve the finite-element system. In other words, not only are there additional unknowns required to pad to a spherical boundary, but the resulting system contains a fully populated submatrix that couples all the boundary unknowns. In the following sections, alternative RBCs are developed that attempt to avoid these drawbacks.

11.4 SURFACE INTEGRAL EQUATION RBC FOR GENERAL BOUNDARY SHAPES

Flexibility in the shape of the outer boundary can be ensured through the use of an RBC based on a surface integral equation. The tangential fields along the boundary of the computational

domain Γ can be related to equivalent surface current densities through

$$\bar{J}_s = \frac{1}{-j\omega\mu}\hat{n} \times (\nabla \times \bar{E}) \tag{11.48}$$

$$\bar{K}_s = \bar{E} \times \hat{n} \tag{11.49}$$

which are suitable if the electric field is the primary unknown and (11.6) is the equation to be solved, or

$$\bar{J}_s = \hat{n} \times \bar{H} \tag{11.50}$$

$$\bar{K}_s = \frac{1}{j\omega\varepsilon}(\nabla \times \bar{H}) \times \hat{n} \tag{11.51}$$

which are suitable for use with (11.7). A robust formulation that avoids the interior resonance problem (Chapter 6) can be obtained from the combined-field equation

$$\begin{aligned}\alpha \bar{E}^{\text{inc}}_{\tan} + (1-\alpha)\eta\hat{n} \times \bar{H}^{\text{inc}} = \alpha\left(-\frac{\nabla\nabla\cdot\bar{A} + k^2\bar{A}}{j\omega\varepsilon} + \hat{n} \times \bar{K}_s + \nabla \times \bar{F}\right)_{\tan} \\ +(1-\alpha)\eta\left(\bar{J}_s - \hat{n} \times \nabla \times \bar{A} - \hat{n} \times \frac{\nabla\nabla\cdot\bar{F} + k^2\bar{F}}{j\omega\mu}\right)\end{aligned} \tag{11.52}$$

where $\bar{A}$ and $\bar{F}$ are the vector potential functions defined in Chapter 1, α is a parameter in the range $0 < \alpha < 1$, and the medium impedance η is used to convert to consistent units and balance the numerical values. The discretization of this type of surface integral equation for a general boundary shape is discussed in Chapter 10, in conjunction with divergence-conforming CN/LT and LN/QT basis functions for the equivalent surface current densities. Using (11.49) and (11.50), a CN/LT representation for the surface currents can be shown to be equivalent to a CT/LN representation for the tangential fields on the boundary. Similarly, an LN/QT representation for the current densities is equivalent to an LT/QN representation for the fields. The compatibility between the divergence-conforming representations introduced for surface integral equations and the curl-conforming basis functions used to discretize the vector Helmholtz equation facilitates the use of an integral equation RBC.

The discretization of (11.52) produces a matrix equation of the form

$$\mathbf{Lk} + \mathbf{Mj} = \mathbf{V}^{\text{inc}} \tag{11.53}$$

where $\mathbf{L}$ and $\mathbf{M}$ are square matrix operators, $\mathbf{k}$ and $\mathbf{j}$ are column vectors containing the coefficients of the basis functions used for the magnetic and electric current densities, respectively, and $\mathbf{V}^{\text{inc}}$ contains weighted samples of the incident fields appearing on the left-hand side of (11.52). Terms in this matrix equation can be rearranged in the form

$$\mathbf{j} = -\mathbf{M}^{-1}\mathbf{Lk} + \mathbf{M}^{-1}\mathbf{V}^{\text{inc}} \tag{11.54}$$

or

$$\mathbf{k} = -\mathbf{L}^{-1}\mathbf{Mj} + \mathbf{L}^{-1}\mathbf{V}^{\text{inc}} \tag{11.55}$$

which provide the desired numerical RBC depending on whether the electric or magnetic field is the primary unknown. The reader is referred to Chapters 9 and 10 for additional information about possible basis and testing functions and their impact on the entries of the

system in (11.53). The specific choice of basis functions does not affect the general form of Equations (11.54) or (11.55).

Using (11.48), the weak Helmholtz equation in (11.6) can be rewritten as

$$\iiint_{\Gamma} \frac{1}{\mu_r} \nabla \times \bar{T} \cdot \nabla \times \bar{E} - k^2 \varepsilon_r \bar{T} \cdot \bar{E} = j\omega\mu_0 \iint_{\partial\Gamma} \bar{T} \cdot \bar{J}_s \tag{11.56}$$

Suppose that the computational domain Γ is divided into tetrahedral cells, and the electric field is represented by a superposition of vector basis functions

$$\bar{E}(x, y, z) \cong \sum_{n=1}^{N_{\text{int}}} e_n \bar{B}_n + \sum_{n=N_{\text{int}}+1}^{N_{\text{int}}+N_{\text{bound}}} e_n \bar{B}_n \tag{11.57}$$

where the basis functions contributing to a tangential field on the boundary $\partial\Gamma$ are separated from the others for convenience. We will assume that the basis functions $\{\bar{B}_n\}$ provide a tangentially continuous representation for $\bar{E}$. It is also necessary to introduce an independent representation for the equivalent surface current density

$$\bar{J}_s \cong \sum_{n=1}^{M_{\text{bound}}} j_n \bar{b}_n \tag{11.58}$$

where the vector basis functions $\{\bar{b}_n\}$ are generally different from those used in (11.57) to represent the electric field. (In most cases, the basis functions $\{\bar{B}_n\}$ are curl conforming while $\{\bar{b}_n\}$ are divergence conforming.) A discretization of the weak Helmholtz equation in (11.56) using testing functions identical to the basis functions in (11.57) throughout the region Γ produces an underdetermined matrix equation

$$\begin{bmatrix} \mathbf{I} & \mathbf{I}_b^T & \mathbf{0} \\ \mathbf{I}_b & \mathbf{B} & \mathbf{J} \end{bmatrix} \begin{bmatrix} \mathbf{e}^{\text{int}} \\ \mathbf{e}^{\text{bound}} \\ \mathbf{j} \end{bmatrix} = \begin{bmatrix} \mathbf{0} \\ \mathbf{0} \end{bmatrix} \tag{11.59}$$

where $\mathbf{I}$, $\mathbf{I}_b$, and $\mathbf{B}$ have entries of the common form

$$I_{mn} = \iiint_{\Gamma} \frac{1}{\mu_r} \nabla \times \bar{B}_m \cdot \nabla \times \bar{B}_n - k^2 \varepsilon_r \bar{B}_m \cdot \bar{B}_n \tag{11.60}$$

and the submatrix $\mathbf{J}$ has entries

$$J_{mn} = -j\omega\mu_0 \iint_{\partial\Gamma} \bar{B}_m \cdot \bar{b}_n \tag{11.61}$$

By incorporating the RBC in (11.54) into the matrix equation, we arrive at the properly determined system

$$\begin{bmatrix} \mathbf{I} & \mathbf{I}_b^T \\ \mathbf{I}_b & \mathbf{B} - \mathbf{J}\mathbf{M}^{-1}\mathbf{L} \end{bmatrix} \begin{bmatrix} \mathbf{e}^{\text{int}} \\ \mathbf{e}^{\text{bound}} \end{bmatrix} = \begin{bmatrix} \mathbf{0} \\ -\mathbf{J}\mathbf{M}^{-1}\mathbf{V}^{\text{inc}} \end{bmatrix} \tag{11.62}$$

where it is assumed that the coefficients $\mathbf{k}$ in (11.54) are the same as those in $\mathbf{e}^{\text{bound}}$ in (11.58). (As an example, this would be possible if a CN/LT representation is used for the magnetic surface current and a CT/LN representation is used for the electric field.) If desired, the procedure can be generalized to use completely unrelated basis functions for these two quantities (Prob. P11.10).

Equation (11.62) is an outward-looking formulation that can be used to describe a general scatterer, with the mesh terminated on an arbitrary boundary enclosing all inhomogeneities. The advantage of an integral equation RBC is that the boundary shape can be

arbitrary and can easily conform to the surface of the scatterer under consideration. Thus, there is no need to pad the mesh to a spherical boundary. However, the submatrices $\mathbf{L}$ and $\mathbf{M}$ in (11.62) are fully populated in general, and as a consequence there is still a substantial amount of fill-in associated with this RBC.

The relative efficiency of a surface integral equation RBC imposed on an arbitrary boundary and the eigenfunction RBC of Section 11.3 imposed on a spherical boundary involves two factors: The eigenfunction RBC requires additional unknowns in order to pad the mesh to a spherical boundary shape, while the surface integral equation RBC involves additional computation associated with the LU factorization required to produce $\mathbf{M}^{-1}$ in (11.62). In an outward-looking formulation, both approaches involve a fully populated submatrix of order equal to the number of boundary unknowns. For a geometry whose boundary is more than a minor perturbation from a sphere, the larger global system required with an eigenfunction RBC is likely to offset the additional computation required to produce $\mathbf{M}^{-1}$ with an integral equation RBC. The disadvantages of these procedures can be mitigated to some extent by an RBC specialized to an axisymmetric radiation boundary (Section 11.6). Furthermore, the trade-offs between these approaches may be somewhat different if they are implemented as inward-looking formulations.

11.5 OUTWARD-LOOKING VERSUS INWARD-LOOKING FORMULATIONS

The preceding sections described outward-looking formulations, where an RBC of some type is used to constrain the vector Helmholtz equation. Since the resulting system has the form of (11.62), containing a dense submatrix, it complicates the matrix solution procedure. Perhaps as a consequence of the partially full, partially sparse matrix structure, most of the three-dimensional outward-looking formulations discussed in the literature employ iterative solution algorithms instead of direct algorithms to solve Equation (11.62).

The alternative inward-looking formulations (Chapter 3) avoid the partially full and partially sparse matrix structure. Inward-looking formulations use the solution of the vector Helmholtz equation to obtain a system constraining tangential fields (or equivalent currents) on the surface of the boundary $\partial\Gamma$, which is then combined with the integral equation in (11.53). For example, given the equivalent electric current $\bar{J}_s$ as the forcing function, (11.59) can be solved to find the equivalent magnetic current $\bar{K}_s$ (or the tangential electric field on $\partial\Gamma$). A repetitive solution for linearly independent currents (say, one basis function at a time) can be used to construct a matrix equation relating $\bar{J}_s$ and $\bar{K}_s$. This system is underdetermined since both $\bar{J}_s$ and $\bar{K}_s$ are unknowns, but it can be combined with (11.53) to produce a properly determined matrix equation. After $\bar{J}_s$ and $\bar{K}_s$ are obtained by the solution of the combined system, (11.59) can be solved again to produce the interior fields. The computational requirements of this approach are that a sparse system representing (11.59) must be solved repetitively to generate a smaller fully populated system relating $\bar{J}_s$ and $\bar{K}_s$, which is then combined with the fully populated system representing (11.53). Thus, the procedure involves a large-order sparse system and a smaller order dense system.

With an inward-looking formulation, an exterior eigenfunction expansion may be more advantageous than it is in the outward-looking case. This is because an eigenfunction series generally provides the minimum number of expansion functions needed to represent the fields in the general case (as compared with typical subsectional representations). Thus,

the inward-looking eigenfunction expansion procedure involves a smaller dense matrix than an inward-looking approach based on a general integral equation representation of the exterior region. (Of course, a spherical eigenfunction expansion requires a mesh that terminates on a spherical boundary, so the sparse matrix for the interior region might be of considerably larger order than that required with an integral equation representation and a general boundary shape.) In both inward- and outward-looking formulations, the use of an eigenfunction expansion eliminates the need to obtain $\mathbf{M}^{-1}$ numerically in order to solve (11.53).

The differences between outward-looking and inward-looking approaches are summarized in Chapter 3 in the context of two-dimensional formulations and are generally that while the inward-looking formulations are easier to implement because they avoid a matrix that is partially sparse and partially full, they are susceptible to uniqueness difficulties since the part of the problem solved first is essentially a closed cavity that might be resonant. (The uniqueness issue is explored for the scalar Helmholtz equation in Section 6.9.) As an alternative to either outward-looking or inward-looking formulations, a third possibility is the combination of (11.53) and (11.59) to produce the system

$$\begin{bmatrix} \mathbf{I} & \mathbf{I}_b^T & \mathbf{0} \\ \mathbf{I}_b & \mathbf{B} & \mathbf{J} \\ \mathbf{0} & \mathbf{L} & \mathbf{M} \end{bmatrix} \begin{bmatrix} \mathbf{e}^{\text{int}} \\ \mathbf{e}^{\text{bound}} \\ \mathbf{j} \end{bmatrix} = \begin{bmatrix} \mathbf{0} \\ \mathbf{0} \\ \mathbf{V}^{\text{inc}} \end{bmatrix} \tag{11.63}$$

Equation (11.63) is neither inward looking nor outward looking and is sparse except for matrix blocks $\mathbf{L}$ and $\mathbf{M}$. This matrix equation eliminates the inward-looking uniqueness difficulties but involves a larger system than (11.62) to solve. The possible advantage to (11.63) is that it simplifies the matrix construction if iterative solution algorithms are used to solve the system. It is particularly advantageous if an axisymmetric radiation boundary (Section 11.6) is employed.

The literature describes several finite-element implementations similar to those considered above. Yuan [9] appears to have been the first to employ the three-dimensional tetrahedral-cell CT/LN functions within an inward-looking scattering formulation, terminated with an integral equation RBC. Yuan presented results for layered spheres that exhibited good agreement with analytical solutions provided that about 10 cells per wavelength were used in the models. Although the uniqueness issue did not appear to impede accurate solutions, it would likely affect the results for electrically larger problems. Reliable inward-looking formulations might be possible, however, if the condition number of the large, sparse system can be monitored to detect fictitious resonances.

Jin and Volakis employed CT/LN functions on hexahedral and tetrahedral cells to represent scattering from a thick slot in a conducting plane, cavity-backed microstrip patch antennas, and other structures [10–12]. Their outward-looking approach used integral equation RBCs to terminate the computational domain along planar boundaries, producing a system similar in matrix structure to (11.62). The use of planar boundaries facilitates an iterative solution of the resulting system, as described in Chapter 4, and they employed a BCG–FFT algorithm. (For general boundary shapes, they modified their approach to use a local RBC similar to those discussed in Section 11.7 instead of the surface integral equation RBC [12].)

Antilla and Alexopoulos developed a similar approach employing CT/LN functions on curved hexahedral cells for the interior fields and CN/LT functions on curved quadrilateral cells for the equivalent boundary currents [13]. (The treatment of curved cells is described

in Section 9.14.) They presented a number of examples showing the accuracy of the formulation and reported that good accuracy was usually obtained with cell densities in the range of 9–12 cells per wavelength.

The preceding approaches involve general three-dimensional scatterers. Lucas and Fontana analyzed periodic structures using an integral equation that incorporated the appropriate Floquet conditions to limit the computational domain to a three-dimensional unit cell [14]. They employed a polynomial-complete quadratic vector representation to discretize the vector Helmholtz equation.

11.6 INTEGRAL EQUATION RBC FOR AXISYMMETRIC BOUNDARY SHAPES

Since the shape of the outer boundary $\partial\Gamma$ used to terminate the computational domain is arbitrary, as long as it fully encloses the scatterer, an alternate possibility is to use an axisymmetric boundary that resides as close to the scatterer as possible. This idea was first proposed by Boyse and Seidl [15] and combines the advantages of the eigenfunction RBC of Section 11.3 and the integral equation RBC of Section 11.4 (the boundary shape remains rather flexible and the numerical inversion of the matrix $\mathbf{M}$ is accomplished more efficiently). As illustrated in Chapter 8, integral equation formulations imposed on axisymmetric surfaces ("body-of-revolution" formulations) can be discretized using cylindrical harmonics to represent the equivalent surface currents. The cylindrical harmonics decouple the resulting equations, creating a block-diagonal structure that substantially reduces the computational complexity required to construct $\mathbf{M}^{-1}$ in an outward-looking formulation (or the dense exterior system arising in an inward-looking approach).

If Equation (11.53) is specialized to an axisymmetric boundary and cylindrical harmonics are used in the representation (Section 8.7), then the equation for the mth harmonic has the form

$$\mathbf{L}_m\mathbf{k} + \mathbf{M}_m\mathbf{j} = \mathbf{V}_m^{\text{inc}} \tag{11.64}$$

and is independent of the equations for the other harmonics. Consequently, the RBC can be found from the solution of the block-diagonal matrix equation

$$\begin{bmatrix} \ddots & 0 & & & \\ 0 & \mathbf{L}_{m-1} & 0 & & \\ & 0 & \mathbf{L}_m & 0 & \\ & & 0 & \mathbf{L}_{m+1} & 0 \\ & & & 0 & \ddots \end{bmatrix} \mathbf{k} + \begin{bmatrix} \ddots & 0 & & & \\ 0 & \mathbf{M}_{m-1} & 0 & & \\ & 0 & \mathbf{M}_m & 0 & \\ & & 0 & \mathbf{M}_{m+1} & 0 \\ & & & 0 & \ddots \end{bmatrix} \mathbf{j} = \mathbf{V}^{\text{inc}} \tag{11.65}$$

Clearly, there are substantial savings arising from (11.65) compared to the larger order, dense matrix equation associated with a general-purpose surface integral equation.

The use of an axisymmetric boundary to truncate the computational domain was first reported by Boyse and Seidl [15, 16] in the context of an inward-looking formulation. Their approach employed node-based Lagrangian expansion functions throughout the interior and cubic-order Hermitian interpolation polynomials to discretize the surface integral equation on the radiation boundary. Cwik et al. [17–19] investigated an inward-looking implementation as well as a formulation based on the matrix structure of (11.63) and used CT/LN functions on tetrahedral cells to discretize the curl–curl equation. Figure 11.3 illustrates the

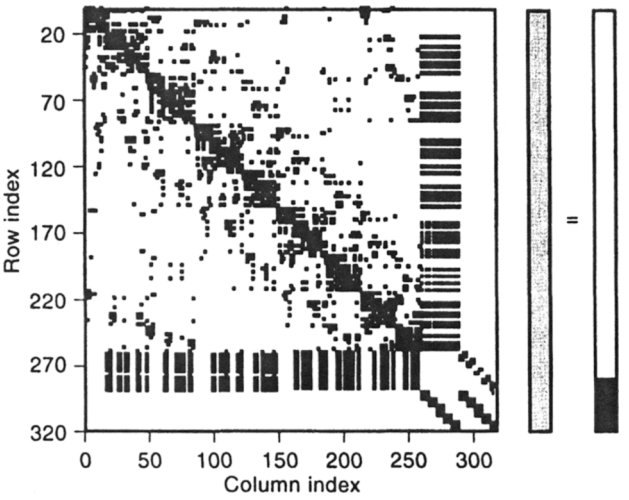

Figure 11.3 Typical matrix structure associated with the formulation illustrated in (11.63) when an axisymmetric integral equation RBC is incorporated. After [19].

typical matrix structure arising from the approach. Because of the block-diagonal structure of (11.65), the resulting global system of equations is almost as sparse as a system obtained from a local RBC. The additional unknowns required to pad the domain to an axisymmetric boundary are likely to be far less than those associated with a spherical boundary and possibly comparable to the small degree of padding required with local RBCs.

11.7 LOCAL RBCS FOR SPHERICAL BOUNDARIES

The computation and storage requirements associated with an eigenfunction RBC (Section 11.3), a general surface integral equation RBC (Section 11.4), or an axisymmetric surface integral equation RBC (Section 11.6) can be quite different and are all largely problem dependent. However, all of these truncation conditions involve global coupling of unknowns around the boundary. To some extent, the overall matrix order and/or the presence of the dense submatrix in (11.62) may limit the problem size amenable to numerical solution using global RBCs. Chapter 3 demonstrated that local RBCs minimize fill-in and can perform well in a variety of situations as long as high accuracy is not required. In this section, local RBCs are developed for three-dimensional scatterers enclosed in spherical boundaries.

Following the procedure that produced the Bayliss–Turkel RBC in the two-dimensional case, consider the outward-propagating field expansion

$$\bar{E}^s(r,\theta,\phi) = \frac{e^{-jkr}}{4\pi r}\sum_{n=0}^{\infty}\frac{\bar{E}_n(\theta,\phi)}{r^n} \tag{11.66}$$

Equation (11.66), known as the Wilcox expansion [20], can be used to represent any outward-propagating field in the region exterior to a three-dimensional scatterer or antenna. In contrast to the similar two-dimensional expansion used in Chapter 3 (which was

an asymptotic approximation), Equation (11.66) can be differentiated term by term and remains uniformly convergent [20].

A family of local RBCs can be developed so that the expansion of (11.66) satisfies the RBC up to some power of $1/r$ [21]. For instance, the standard radiation condition operator applied to (11.66) leaves a residual

$$\hat{r} \times \nabla \times \bar{E}^s - jk\bar{E}^s = \frac{e^{-jkr}}{4\pi r} \sum_{n=0}^{\infty} \left(-jk \frac{\hat{r}(\hat{r} \cdot \bar{E}_n)}{r^n} + \frac{r\nabla(\hat{r} \cdot \bar{E}_n) + n\bar{E}_n^{\tan}}{r^{n+1}} \right) \tag{11.67}$$

Using the vector identities

$$\hat{r} \times (r\nabla \times \bar{E}_n) = r\nabla(\hat{r} \cdot \bar{E}_n) - \bar{E}_n^{\tan} \tag{11.68}$$

$$\hat{r} \times (\hat{r} \times \bar{E}_n) = -\bar{E}_n^{\tan} \tag{11.69}$$

where

$$\bar{E}_n^{\tan} = \bar{E}_n - \hat{r}(\hat{r} \cdot \bar{E}_n) \tag{11.70}$$

and the fact that $\bar{E}$ has zero divergence in this region, which implies that $\hat{r} \cdot \bar{E}_0 = 0$, it follows that the residual on the right-hand side of (11.67) is $O(r^{-2})$ as $r \to \infty$.

The leading-order behavior of the residual suggests modifications in the operator that can reduce the residual to a more rapidly decaying power of r and ensure a more accurate RBC for large r. For instance, the alternative operator

$$\hat{r} \times \nabla \times \bar{E}^s - jk\bar{E}^s_{\tan} = \frac{e^{-jkr}}{4\pi r} \sum_{n=0}^{\infty} \frac{r\nabla(\hat{r} \cdot \bar{E}_n) + n\bar{E}_n^{\tan}}{r^{n+1}} \tag{11.71}$$

has a residual with leading-order behavior $O(r^{-3})$. The operator

$$\begin{aligned} &[\hat{r} \times (\nabla \times) - jk][\hat{r} \times \nabla \times \bar{E}^s - jk\bar{E}^s_{\tan}] \\ &= \frac{e^{-jkr}}{4\pi r} \sum_{n=1}^{\infty} (n+1) \frac{r\nabla(\hat{r} \cdot \bar{E}_n) + n\bar{E}_n^{\tan}}{r^{n+2}} \end{aligned} \tag{11.72}$$

produces a residual of $O(r^{-4})$. Furthermore, the modified operator

$$\begin{aligned} &\left[\hat{r} \times (\nabla \times) - jk - \frac{2}{r}\right][\hat{r} \times \nabla \times \bar{E}^s - jk\bar{E}^s_{\tan}] \\ &= \frac{e^{-jkr}}{4\pi r} \sum_{n=1}^{\infty} (n-1) \frac{r\nabla(\hat{r} \cdot \bar{E}_n) + n\bar{E}_n^{\tan}}{r^{n+2}} \end{aligned} \tag{11.73}$$

produces a residual of $O(r^{-5})$. This process can be continued indefinitely [21].

A "first-order" RBC is obtained by equating the left-hand side of (11.71) to zero. The second-order RBC can be obtained from the left-hand side of (11.73), which can be rewritten in the form

$$\hat{r} \times \nabla \times \bar{E}^s = jk\bar{E}^s_{\tan} + \beta(r)\nabla \times [\hat{r}(\hat{r} \cdot \nabla \times \bar{E}^s)] + jk\beta(r)\nabla^{\tan}(\hat{r} \cdot \bar{E}^s) \tag{11.74}$$

where

$$\beta(r) = \frac{1}{2jk + 2/r} \tag{11.75}$$

Because of the first-derivative term in (11.74), its direct implementation within a finite-element discretization of the weak equation in (11.6) produces a nonsymmetric matrix equation. However, the relation

$$E_r^s = \frac{1}{k^2}\hat{r}\cdot\nabla\times\nabla\times\bar{E}^s = -\frac{1}{k^2}\nabla\cdot[\hat{r}\times(\nabla\times\bar{E}^s)] \cong -\frac{j}{k}\nabla\cdot\bar{E}_{\tan}^s \tag{11.76}$$

can be incorporated into the final term in (11.74) to produce

$$\hat{r}\times\nabla\times\bar{E}^s \cong jk\bar{E}_{\tan}^s + \beta(r)\nabla\times[\hat{r}(\hat{r}\cdot\nabla\times\bar{E}^s)] + \beta(r)\nabla^{\tan}(\nabla\cdot\bar{E}_{\tan}^s) \tag{11.77}$$

Equation (11.77) preserves the symmetry of the finite-element matrix operator and is only slightly less accurate than (11.74) [22]. [However, as discussed below, the third term on the right-hand side of (11.77) is problematic for use with curl-conforming basis functions.]

The second-order RBCs in (11.74) and (11.77) can be thought of as special cases of a more general RBC suggested by Webb and Kanellopoulos [23], which has the form

$$\begin{aligned}\hat{r}\times\nabla\times\bar{E}^s \cong{}& jk\bar{E}_{\tan}^s + \beta(r)\nabla\times[\hat{r}(\hat{r}\cdot\nabla\times\bar{E}^s)] \\ &+(s-1)\beta(r)\nabla^{\tan}(\nabla\cdot\bar{E}_{\tan}^s) + (2-s)jk\beta(r)\nabla^{\tan}(\hat{r}\cdot\bar{E}^s)\end{aligned} \tag{11.78}$$

where s is an arbitrary parameter. The choice $s = 1$ produces (11.74), while the choice $s = 2$ yields (11.77).

The relative accuracy of the RBCs in (11.74), (11.77), and (11.78) can be investigated by applying them to the spherical vector wave functions in (11.38) and (11.39), which represent outward-propagating fields and should satisfy an exact RBC. The error in all the RBCs is independent of the index m in (11.38) and (11.39) but increases as the index n increases for a fixed boundary radius [22]. The performance of the second-order RBCs is generally far better than the first-order RBC obtained from (11.71). The part of the second-order condition involving the operator

$$\nabla\times[\hat{r}(\hat{r}\cdot\nabla\times\bar{E}^s)] \tag{11.79}$$

is only associated with the TE-to-r part of the field, while the operators

$$\nabla^{\tan}(\nabla\cdot\bar{E}_{\tan}^s) \tag{11.80}$$

$$\nabla^{\tan}(\hat{r}\cdot\bar{E}^s) \tag{11.81}$$

only involve the TM-to-r part of the field. Thus, these terms are of essentially equal importance in these conditions. The conditions (11.74), (11.77), and (11.78) only differ in the TM-to-r part of the field. Furthermore, the RBC in (11.78) exhibits the best accuracy for a choice of s somewhere between 0 and 1, rather than either $s = 1$ or $s = 2$ [22]. Figure 11.4 shows the error in the various RBCs for a mode with $n = 5$ as a function of the boundary location r.

The local RBCs in (11.74)–(11.78) must be imposed on a spherical boundary surrounding the scatterer. Consider (11.77). If substituted into the boundary integral in (11.6), under the assumption that $\mu_r = 1$ along the boundary, the boundary integral assumes the

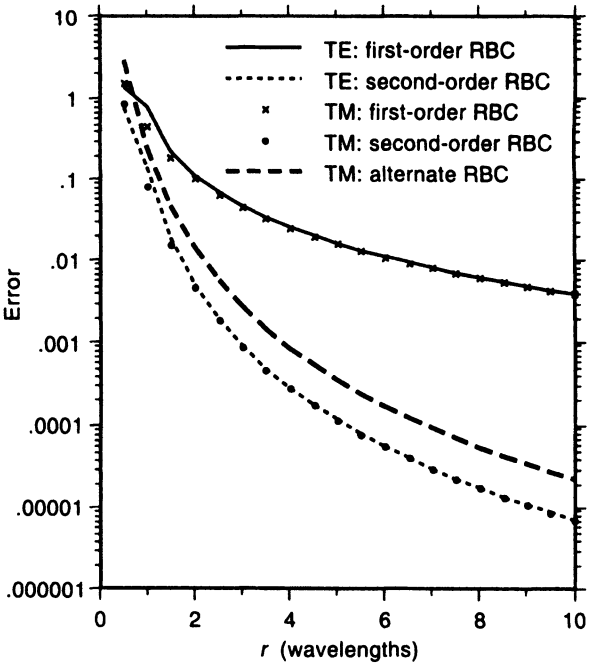

Figure 11.4 Error in the TE and TM parts of the first- and second-order local RBCs plotted as a function of the radius of the radiation boundary for the $n = 5$ spherical harmonic. After [22]. ©1992 IEEE.

form

$$\iint_{\partial\Gamma} \bar{T}\cdot\hat{n}\times\nabla\times\bar{E}^s = jk\iint_{\partial\Gamma}\bar{T}\cdot\bar{E}^s_{\tan}$$
$$+\beta(r)\iint_{\partial\Gamma}\bar{T}\cdot\nabla\times[\hat{r}(\hat{r}\cdot\nabla\times\bar{E}^s)] \qquad (11.82)$$
$$+\beta(r)\iint_{\partial\Gamma}\bar{T}\cdot\nabla^{\tan}(\nabla\cdot\bar{E}^s_{\tan})$$

Using the vector identities

$$\bar{T}\cdot\nabla\times\bar{A} = \nabla\times\bar{T}\cdot\bar{A} - \nabla\cdot(\bar{T}\times\bar{A}) \qquad (11.83)$$

$$\nabla\cdot(\Psi\bar{T}) = \Psi\nabla\cdot\bar{T} + \nabla\Psi\cdot\bar{T} \qquad (11.84)$$

and invoking the two-dimensional divergence theorem, Equation (11.82) can be rewritten as

$$\iint_{\partial\Gamma} \bar{T}\cdot\hat{n}\times\nabla\times\bar{E}^s = jk\iint_{\partial\Gamma}\bar{T}\cdot\bar{E}^s_{\tan}$$
$$+\beta(r)\iint_{\partial\Gamma}(\hat{r}\cdot\nabla\times\bar{T})(\hat{r}\cdot\nabla\times\bar{E}^s) \qquad (11.85)$$
$$-\beta(r)\iint_{\partial\Gamma}(\nabla\cdot\bar{T}_{\tan})(\nabla\cdot\bar{E}^s_{\tan})$$

The form of (11.85) spreads the derivatives among the basis and testing functions and, for testing functions identical to the basis functions, produces a symmetrical matrix operator after discretization.

In the development of (11.85), we tacitly assume that the necessary derivatives exist. However, if we subsequently expand the field in terms of curl-conforming basis functions such as the CT/LN or LT/QN functions considered in Section 11.2, this assumption is violated. The basis and testing functions do not maintain normal continuity from cell to cell along the radiation boundary, and thus the third integral on the right-hand side of (11.85) contains the product of two Dirac delta–like functions located along cell edges. This behavior is a direct consequence of the curl-conforming representation and not a fundamental limitation of the equations leading to (11.85). One way of avoiding this difficulty is to simply omit the third integral. As noted above, however, the second and third expressions are expected to be equally important in the RBC, and omitting the third integral should reduce the overall accuracy to that of the first-order RBC. A better remedy might be to employ a continuous representation for the fields along the radiation boundary, as suggested by Kanellopoulos and Webb [24]. Since a continuous representation throughout the interior might severely distort the nullspace eigenfunctions, a curl-conforming interior expansion must transition to a continuous basis confined to $\partial\Gamma$. The continuous boundary expansion permits the evaluation of all terms in (11.85) without difficulty.

A third remedy is suggested by Savage [25], who implemented a procedure for projecting the curl-conforming representation onto a divergence-conforming representation defined on the same finite-element mesh. The problematical term in (11.85) is evaluated using the divergence-conforming functions, and the result is projected back onto the curl-conforming space. Although the accuracy of the RBC implementation improves, the projection process causes the support of an individual basis function to spread into neighboring cells, resulting in additional matrix fill-in. [If the projection process is used with tetrahedral-cell CT/LN functions, there may be 27 nonzero matrix entries per row due to the third integral in (11.85), compared with 5 nonzero entries due to the first and second integrals.]

A more general remedy would be obtained through the use of dual interlocking meshes simultaneously supporting both curl-conforming and divergence-conforming expansions that share common coefficients. Except for structured quadrilateral grids, such a scheme would require vector expansion functions defined on general polygonal shapes (for instance, the dual grid associated with a triangular-cell mesh would not be triangular).

To summarize the local RBC approach, the weak equation can be combined with the RBC in (11.77), after which terms involving the incident field can be added and subtracted from the boundary integral to produce

$$\begin{aligned}
&\iiint_{\Gamma} \frac{1}{\mu_r} \nabla \times \bar{T} \cdot \nabla \times \bar{E} - k^2 \varepsilon_r \bar{T} \cdot \bar{E} + jk \iint_{\partial\Gamma} \bar{T} \cdot \bar{E}_{\tan} \\
&\quad + \beta(r) \iint_{\partial\Gamma} (\hat{r} \cdot \nabla \times \bar{T})(\hat{r} \cdot \nabla \times \bar{E}) - (\nabla \cdot \bar{T}_{\tan})(\nabla \cdot \bar{E}_{\tan}) \\
&\quad = -\iint_{\partial\Gamma} [\bar{T} \cdot \hat{r} \times \nabla \times \bar{E}^{\text{inc}} - jk \bar{T} \cdot \bar{E}^{\text{inc}}_{\tan} \\
&\qquad\qquad - \beta(r) \bar{T} \cdot \nabla \times (\hat{r}\hat{r} \cdot \nabla \times \bar{E}^{\text{inc}}) + \beta(r) \bar{T} \cdot \nabla^{\tan} (\nabla \cdot \bar{E}^{\text{inc}}_{\tan})]
\end{aligned} \tag{11.86}$$

which is entirely in terms of the total electric field as the primary unknown. The electric

field can be expanded in curl-conforming basis functions, and the same functions can be used for the testing functions, provided that some means of implementing the divergence operator is developed. The remaining restriction on (11.86) is the spherical shape of the radiation boundary.

Preliminary numerical testing of local RBCs for spherical targets was reported in [26, 27], and the first extensive application of the approach appeared in [28] and is summarized in [8] and [12]. Figure 11.5 shows the bistatic scattering cross section of a perfectly conducting cube of side dimension 0.755λ, obtained using approximately 33,000 tetrahedral-cell CT/LN basis functions and the RBC in (11.77). In this case, the RBC was located only 0.1λ from the corners of the cube. Although references [8, 12, 28] claim to employ the second-order RBC in (11.77), it appears that the implementation omitted the third integral in (11.85) and thus may only be as accurate as a first-order RBC.

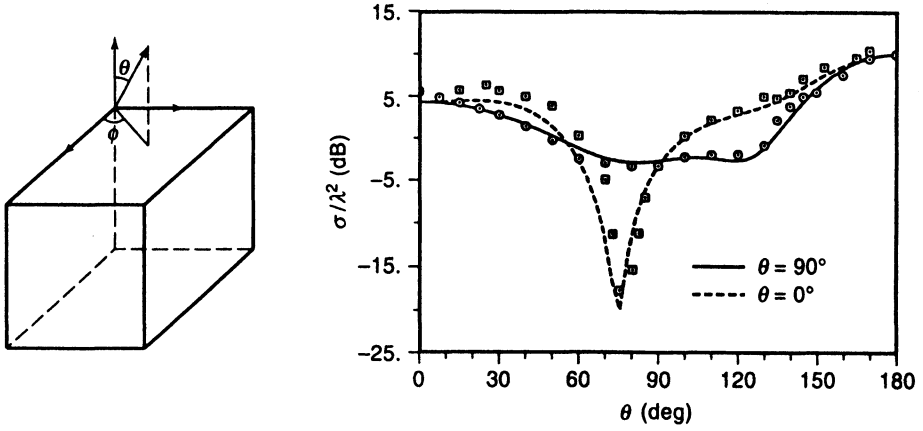

Figure 11.5 Bistatic scattering cross section of a conducting cube of side dimension 0.755λ. Lines represent the result from the CT/LN discretization of the vector Helmholtz equation; circles and squares denote measured data for comparison. After [28]. ©1993 IEEE.

Although local RBCs are approximate, they offer the possibility of terminating the computational domain with little or no fill-in beyond that associated with the vector Helmholtz equation. In many applications, they appear to be sufficiently accurate. The restriction to a spherical boundary places an unacceptable burden on the approach, however, and the following section considers the extension of local RBCs to more general boundary shapes.

11.8 LOCAL RBCS FOR GENERAL THREE-DIMENSIONAL BOUNDARY SHAPES

Since the task of padding the computational domain to a spherical boundary might introduce an unacceptably large number of unknowns, RBCs applicable to more general boundary shapes are desired. Development of RBCs is a recent endeavor, and the testing and evaluation of three-dimensional RBCs to date is far from extensive. Consequently, at the time of

this writing it is impossible to survey the local RBCs that have been suggested for general boundary shapes and assess their relative accuracy with any confidence. In this section, several RBCs proposed for general boundaries are briefly surveyed.

As a first choice, the local RBC in (11.77) can be extended to piecewise-planar boundaries by the simple expedient of replacing the spherical normal vector $\hat{r}$ with the general normal vector $\hat{n}$ and replacing the factor $1/r$ in the coefficients with the local curvature (zero). This produces the RBC [28]

$$\hat{n} \times \nabla \times \bar{E}^s = jk\bar{E}^s_{\tan} + \frac{1}{2jk}\nabla \times [\hat{n}(\hat{n} \cdot \nabla \times \bar{E}^s)] + \frac{1}{2jk}\nabla^{\tan}(\nabla \cdot \bar{E}^s_{\tan}) \tag{11.87}$$

One might expect a decrease in the accuracy of the RBC after such a substitution, but reports suggest that good results can still be obtained even if the RBC is less than $\lambda/3$ from the scatterer [8, 28].

D'Angelo and Mayergoyz investigated the second-order Engquist–Majda RBC within a three-dimensional formulation employing CT/LN functions and piecewise-planar boundaries [29, 30]. Along a locally planar boundary, the RBC is equivalent to

$$\hat{n} \times \nabla \times \bar{E}^s = jk\bar{E}^s_{\tan} + \frac{j}{2k}\left(\frac{\partial^2 \bar{E}^s_{\tan}}{\partial t^2} + \frac{\partial^2 \bar{E}^s_{\tan}}{\partial u^2}\right) + \nabla^{\tan}(\hat{n} \cdot \bar{E}^s) \tag{11.88}$$

where (t, u) denote the tangential variables. D'Angelo and Mayergoyz suggested locating the radiation boundary approximately 1λ from the scatterer surface.

Sun and Balanis proposed an alternative family of vector RBCs that were derived from one-way wave equations [31]. Their second-order RBC, applicable to general piecewise-planar boundaries, has the form

$$\begin{aligned} \hat{n} \times \nabla \times \bar{E}^s = {} & jkp_0\bar{E}^s_{\tan} + q_0\nabla^{\tan}(\hat{n} \cdot \bar{E}^s) \\ & - \frac{jp_1}{k}\nabla \times [\hat{n}(\hat{n} \cdot \nabla \times \bar{E}^s)] + \frac{jp_2}{k}\nabla^{\tan}(\nabla \cdot \bar{E}^s_{\tan}) \end{aligned} \tag{11.89}$$

where the parameters q_0, p_0, p_1, and p_2 are to be obtained by approximating the pseudo-differential operator according to

$$\begin{aligned} & \sqrt{k^2\bar{\bar{I}} - \nabla^{\tan} \times \nabla^{\tan} \times + \nabla^{\tan}\nabla^{\tan}\cdot} \\ & \approx k(p_0\bar{\bar{I}} - p_1\nabla^{\tan} \times \nabla^{\tan} \times + p_2\nabla^{\tan}\nabla^{\tan}\cdot) \end{aligned} \tag{11.90}$$

for the specific boundary of interest. The details of pseudo-differential operator theory are beyond the scope of this text. However, for planar boundaries, a Padé approximation of this operator produces $q_0 = 0.75$, $p_0 = 1$, $p_1 = 0.5$, and $p_2 = 0.25$ for use with (11.89) [31]. These values are reported to produce minimal reflections from planar boundaries over a wide range of incident angles.

It is noteworthy that the three RBCs in (11.87), (11.88), and (11.89) differ only slightly from each other when applied to piecewise-planar boundaries. One might expect that an RBC applicable to continuously curved boundaries would have a similar form, such as

$$\hat{n} \times \nabla \times \bar{E}^s = \bar{\bar{\alpha}} \cdot \bar{E}^s_{\tan} + \bar{\bar{\delta}}\nabla \times [\hat{n}(\hat{n} \cdot \nabla \times \bar{E}^s)] + \bar{\bar{\gamma}}\nabla^{\tan}(\nabla \cdot \bar{E}^s_{\tan}) \tag{11.91}$$

where $\bar{\bar{\alpha}}$, $\bar{\bar{\delta}}$, and $\bar{\bar{\gamma}}$ might be tensor or scalar quantities that are functions of the boundary curvature. The RBCs of this form have been proposed by Stupfel [32] and Chatterjee and

Volakis [33, 34]. Stupfel suggests the parameters [32]

$$\bar{\bar{\alpha}} = \frac{1}{2(jk + 2\kappa_m)} \left[-2k^2 + (3\kappa_2 + \kappa_1)\left(jk + \frac{\kappa_2 - \kappa_1}{4} \right) \hat{t}_1\hat{t}_1 + (3\kappa_1 + \kappa_2)\left(jk - \frac{\kappa_2 - \kappa_1}{4} \right) \hat{t}_2\hat{t}_2 \right] \tag{11.92}$$

and

$$\delta = \gamma = \frac{1 - j\kappa_m/k}{2(jk + 2\kappa_m)} \tag{11.93}$$

while Chatterjee and Volakis suggest [33, 34]

$$\bar{\bar{\alpha}} = \delta \{4\kappa_m^2 - \kappa_g + jkD + [\kappa_1^2 + \kappa_m(\kappa_1 - \kappa_2) - \kappa_1 D]\hat{t}_1\hat{t}_1 + [\kappa_2^2 + \kappa_m(\kappa_2 - \kappa_1) - \kappa_2 D]\hat{t}_2\hat{t}_2\} \tag{11.94}$$

$$\delta = \frac{1}{D - 2\kappa_m} \tag{11.95}$$

and

$$\bar{\bar{\gamma}} = \frac{\delta}{jk}\left(jk + 3\kappa_m - \frac{\kappa_g}{\kappa_m} - 2(\kappa_1\hat{t}_1\hat{t}_1 + \kappa_2\hat{t}_2\hat{t}_2) \right) \tag{11.96}$$

In these expressions, $\hat{n}$ denotes the normal vector to the boundary, κ_1 and κ_2 denote the principal curvatures of the boundary, $\kappa_g = \kappa_1\kappa_2$ is the Gaussian curvature, $\kappa_m = \frac{1}{2}(\kappa_1 + \kappa_2)$ is the mean curvature, and

$$D = 2jk + 5\kappa_m - \frac{\kappa_g}{\kappa_m} \tag{11.97}$$

The expressions for $\bar{\bar{\alpha}}$ in (11.92) and (11.94) and $\bar{\bar{\gamma}}$ in (11.96) are tensor quantities. The parameters in (11.92) and (11.93) apparently neglect derivatives of the curvature while (11.94)–(11.96) take curvature derivatives into account [32–34]. If these parameters are specialized to a spherical boundary shape, both choices simplify to produce the spherical RBC in (11.77).

11.9 RBCS BASED ON FICTITIOUS ABSORBERS

An alternate way of truncating the computational domain in an open-region problem is to surround it with a high-loss medium. Beyond a region of lossy material sufficient to absorb most of the energy, the region can be terminated in a perfect electric or magnetic wall or in a local RBC appropriate for that material. While physically realizable absorbing materials would work in principle, they generally require the introduction of a relatively large number of additional unknowns. Better performance can be realized through the use of fictitious materials that are nonphysical and possibly active [8, 35]. Recently, this idea was extended to the use of a nonphysical anisotropic material that in principle (prior to truncation and discretization) would absorb uniform plane waves from any angle without reflection [36]. Such a material is known as a *perfectly matched layer* (PML).

For instance, consider a medium with relative permittivity and permeability tensors of the form

$$\bar{\bar{\varepsilon}}_r = \bar{\bar{\mu}}_r = \begin{bmatrix} 1 - j\dfrac{\sigma}{\omega\varepsilon} & 0 & 0 \\ 0 & 1 - j\dfrac{\sigma}{\omega\varepsilon} & 0 \\ 0 & 0 & \left(1 - j\dfrac{\sigma}{\omega\varepsilon}\right)^{-1} \end{bmatrix} \tag{11.98}$$

Assuming that the interface between free space and an infinite half-space with the medium parameters given in (11.98) is located at $z = 0$, a wave incident at an arbitrary angle is perfectly absorbed (Prob. P11.20) for both perpendicular polarization,

$$\bar{E}^{\text{inc}} = \hat{y} E_0 e^{-jk(x \sin\theta + z\cos\theta)} \tag{11.99}$$

and for parallel polarization,

$$\bar{H}^{\text{inc}} = \hat{y} H_0 e^{-jk(x \sin\theta + z\cos\theta)} \tag{11.100}$$

or any linear combination thereof. Therefore, if the loss tangent in (11.98) is adjusted appropriately, a relatively small region of such a material (typically much less than a free-space wavelength) will sufficiently absorb an incident wave with minimal reflections. For a numerical implementation, the fields in the absorbing region may be represented using the same basis functions that are employed throughout the rest of the computational domain. Beyond the absorber, the region can be terminated with a perfectly conducting wall or some type of local absorbing boundary condition.

Fictitious absorbing materials appear to provide much lower reflections than the local RBCs discussed in preceding sections without substantial computational overhead [36–39]. They have been used with the finite-difference time-domain method [36, 37] and with frequency-domain discretizations of the vector Helmholtz equation [38–39]. To date, a detailed comparison of their accuracy and relative computational costs with those of the RBCs discussed in previous sections has not been performed.

11.10 VECTOR FORMULATION FOR AXISYMMETRIC HETEROGENEOUS SCATTERERS

The preceding formulations are capable of treating fairly arbitrary isotropic geometries. A heterogeneous scatterer with rotational symmetry, that is, μ_r and ε_r, which do not vary with ϕ, can be treated by a more efficient process that only involves unknowns along a generating sector (Figure 11.6). If the excitation is also rotationally symmetric, as considered in Section 8.8, the formulation is particularly simple since the primary unknown is a single ϕ-component of one of the fields. For a general excitation, a formulation in terms of two ϕ-components (or in terms of the closely related *coupled azimuthal potentials*) is possible [40–42]. It is also possible to pose the problem in terms of a formulation involving three components of a single field [43, 44]. In this section, we review a formulation similar to [44] involving the electric field as the primary unknown.

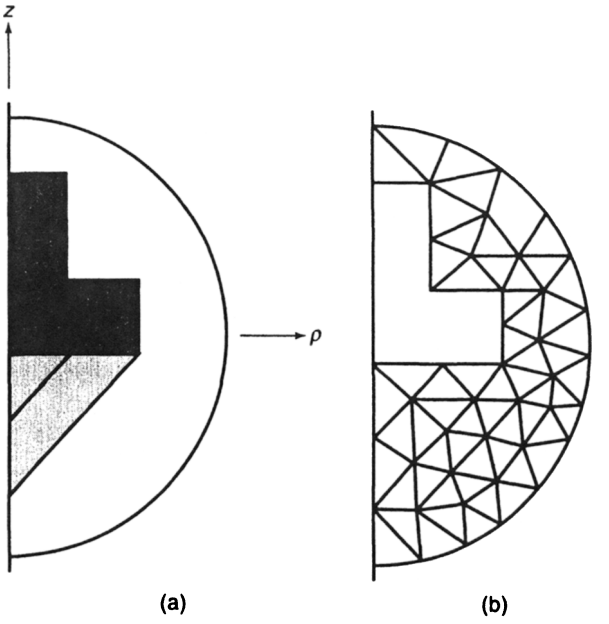

Figure 11.6 (a) Generating sector for an axisymmetric object. (b) Triangular cell mesh for the generating sector.

If the geometry is rotationally symmetric about the z-axis in a cylindrical coordinate system, the electric field can be written in the form

$$\bar{E}(\rho, \phi, z) = \sum_{m=-\infty}^{\infty} \left[\bar{E}_t(\rho, z) + \hat{\phi} E_\phi(\rho, z)\right] e^{jm\phi} \tag{11.101}$$

where the ρ–z plane will be considered the "transverse" plane. The harmonics in (11.101) are coupled only by the excitation. Applied to a single harmonic, the vector Helmholtz equation (11.1) has ϕ-component

$$-\tilde{\nabla} \cdot \left(\frac{1}{\rho \mu_r} \tilde{\nabla}(\rho E_\phi)\right) + jm\tilde{\nabla} \cdot \left(\frac{1}{\rho \mu_r} \bar{E}_t\right) - k^2 \varepsilon_r E_\phi = 0 \tag{11.102}$$

and transverse component

$$\nabla \times \left(\frac{1}{\mu_r} \nabla \times \bar{E}_t\right) + \frac{jm}{\rho^2 \mu_r} \tilde{\nabla}(\rho E_\phi) - \left(k^2 \varepsilon_r - \frac{m^2}{\rho^2 \mu_r}\right) \bar{E}_t = 0 \tag{11.103}$$

where we have suppressed the ϕ-dependence and introduced the pseudo-∇-operator defined by

$$\tilde{\nabla} \Psi = \hat{\rho} \frac{\partial \Psi}{\partial \rho} + \hat{z} \frac{\partial \psi}{\partial z} \tag{11.104}$$

and

$$\tilde{\nabla} \cdot \bar{A} = \frac{\partial A_\rho}{\partial \rho} + \frac{\partial A_z}{\partial z} \tag{11.105}$$

Note that the ordinary curl operator $\nabla\times$ is used in (11.103).

Multiplying (11.102) by a scalar testing function T and integrating over the volume of the three-dimensional region produce the weak equation

$$\int_\rho \int_z \left(\frac{1}{\rho\mu_r} \tilde{\nabla} T \cdot \tilde{\nabla}(\rho E_\phi) - \frac{jm}{\rho\mu_r} \tilde{\nabla} T \cdot \bar{E}_t - \frac{k^2 \varepsilon_r}{\rho} T(\rho E_\phi) \right) \rho \, d\rho \, dz$$
$$= \int_{\partial\Gamma} \left(\frac{1}{\rho\mu_r} T \frac{\partial(\rho E_\phi)}{\partial n} - \frac{jm}{\rho\mu_r} T \hat{n} \cdot \bar{E}_t \right) \rho \, dt \tag{11.106}$$

where t is a local variable tangential to the boundary of the generating sector and the ϕ-integration has been evaluated and omitted (as if the testing function had the appropriate ϕ-dependence). Similarly, multiplying (11.103) with a vector testing function oriented in the transverse (ρ–z) plane and integrating over the volume lead to the weak equation

$$\int_\rho \int_z \left[\frac{1}{\mu_r} \nabla \times \bar{T} \cdot \nabla \times \bar{E}_t + \frac{jm}{\rho^2 \mu_r} \bar{T} \cdot \tilde{\nabla}(\rho E_\phi) - \left(k^2 \varepsilon_r - \frac{m^2}{\rho^2 \mu_r} \right) \bar{T} \cdot \bar{E}_t \right] \rho \, d\rho \, dz$$
$$= - \int_{\partial\Gamma} \frac{1}{\mu_r} (\bar{T} \cdot \hat{n} \times \nabla \times \bar{E}_t) \rho \, dt \tag{11.107}$$

The form of the preceding equations suggests that (ρE_ϕ) and $\bar{E}_t$ be represented by independent expansions, such as

$$\rho E_\phi(\rho, z) \cong \sum_{n=1}^{N_s} e_{\phi n} B_n(\rho, z) \tag{11.108}$$

and

$$\bar{E}_t(\rho, z) \cong \sum_{n=1}^{N_v} e_{tn} \bar{B}_n(\rho, z) \tag{11.109}$$

where $\{B_n\}$ denote scalar Lagrangian basis functions while $\{\bar{B}_n\}$ denote curl-conforming vector basis functions in the transverse (ρ–z) plane. For instance, the generating sector can be modeled by triangular cells (Figure 11.6) and the usual triangular-cell basis functions can be incorporated. The use of ρE_ϕ as the primary scalar unknown is not only convenient, it appears to be essential to achieve a proper representation of the nullspace of the curl–curl operator [44].

Boundary conditions must be imposed along the $\rho = 0$ axis, the outer radiation boundary, and the surface of any imbedded perfect conductors. Along the axis, the boundary conditions are $\rho E_\phi = 0$ and $\hat{\rho} \times (\nabla \times \bar{E}_t) = 0$. At the surface of perfect electric conductors, the appropriate conditions are $\rho E_\phi = 0$ and $\hat{n} \times \bar{E}_t = 0$. Along the radiation boundary, some type of RBC must be combined with the weak equations. Observe that the ϕ-component of $\hat{n} \times (\nabla \times \bar{E}^s)$, for the mth harmonic, can be written as

$$\hat{\phi} \cdot \hat{n} \times \nabla \times \bar{E}^s = -\frac{1}{\rho} \frac{\partial(\rho E_\phi^s)}{\partial n} + \frac{jm}{\rho} \hat{n} \cdot \bar{E}_t^s \tag{11.110}$$

which is exactly the expression appearing in the boundary integral in (11.106). Thus, local or global RBCs can be implemented in the usual manner (after separating the transverse and ϕ-components) by substitution into the boundary integrals in (11.106) and (11.107).

Several axisymmetric formulations have been reported. Morgan et al. [40] developed an inward-looking formulation in terms of coupled azimuthal potentials, where an

eigenfunction series was used to represent fields in the exterior region. Gordon and Mittra [41] used coupled azimuthal potentials and developed local RBCs based on the series in (11.66). Hoppe et al. [42] discuss several ways of incorporating integral equation RBCs into an axisymmetric formulation employing the ϕ-components of the fields as primary unknowns, which are represented by the usual scalar Lagrangian functions. Khebir et al. [43] used a node-based Lagrangian expansion that treated all three components of the field as independent unknowns but employed the local RBC in (11.77) on a spherical boundary. Their results suggest that the local RBC works well for a variety of scatterers. Reference [44] appears to be the first to use a formulation similar to that outlined above, where scalar and vector basis functions are used for the ϕ-component and transverse components, respectively, of a single field. However, [44] only considered closed-region applications.

11.11 ALTERNATIVE FORMULATIONS FOR THREE-DIMENSIONAL SCATTERING

Previous sections of this chapter have considered formulations based on the vector Helmholtz equations in (11.1) and (11.2), with discretizations obtained from the curl-conforming vector basis functions developed in Chapter 9. Because scalar representations are widely used in other engineering disciplines and are compatible with a substantial amount of general-purpose finite-element software, including field display tools, much interest remains in three-dimensional electromagnetic formulations that permit the use of node-based Lagrangian basis functions. Because of the nature of electromagnetic fields, however (such as the jump discontinuities at material interfaces), such formulations must involve auxiliary potential functions as the primary unknowns instead of the vector fields. Approaches based on potential functions have been discussed by several authors [45–48]; one based on [46] is briefly summarized below.

Suppose we wish to solve Maxwell's equations (1.1)–(1.4) within a source-free three-dimensional region Γ, subject to boundary conditions that specify tangential $\bar{E}$ on a part of the boundary ($\partial\Gamma_1$) and tangential $\bar{H}$ on the rest ($\partial\Gamma_2$). By introducing a vector potential function $\bar{A}$ and a scalar potential function Φ that satisfy

$$\bar{H} = \frac{1}{\mu}\nabla \times \bar{A} \tag{11.111}$$

$$\bar{E} = -j\omega\bar{A} - \nabla\Phi \tag{11.112}$$

one readily obtains the differential equations

$$\nabla \times \left(\frac{1}{\mu}\nabla \times \bar{A}\right) - \omega^2\varepsilon\left(\bar{A} + \frac{1}{j\omega}\nabla\Phi\right) = 0 \tag{11.113}$$

and

$$\nabla \cdot \varepsilon\left(\bar{A} + \frac{1}{j\omega}\nabla\Phi\right) = 0 \tag{11.114}$$

to be satisfied by the potential functions. There is a remaining degree of freedom not

specified in (11.111) and (11.112); the choice

$$\nabla \cdot \bar{A} = -j\omega\varepsilon\mu\Phi \tag{11.115}$$

ensures the continuity of both the vector and scalar potential functions at material interfaces [46]. Substitution of (11.115) into the previous equations yields

$$\nabla \times \left(\frac{1}{\mu}\nabla \times \bar{A}\right) - \nabla\left(\frac{1}{\mu}\nabla \cdot \bar{A}\right) - \omega^2\varepsilon\bar{A} - j\omega\Phi\nabla\varepsilon = 0 \tag{11.116}$$

and

$$-\nabla \cdot (\varepsilon\nabla\Phi) - \omega^2\varepsilon^2\mu\Phi - j\omega\bar{A} \cdot \nabla\varepsilon = 0 \tag{11.117}$$

as equations that must be solved to produce the potential functions. Since $\bar{A}$ and Φ are continuous quantities, these equations are appropriate for finite-element discretization using Lagrangian basis functions. In general, there are four unknowns per node associated with the representation. Once the potential functions are determined, the fields can be constructed using (11.111) and (11.112).

Boundary conditions on the fields at conducting surfaces and radiation boundaries must be translated into boundary conditions on the potential functions. On the part of the boundary where the tangential electric field is specified ($\partial\Gamma_1$), appropriate conditions on the potential functions are

$$\hat{n} \times \bar{A} = -\frac{1}{j\omega}\hat{n} \times \bar{E} \tag{11.118}$$

$$\nabla \cdot \bar{A} = 0 \tag{11.119}$$

$$\Phi = 0 \tag{11.120}$$

while on the part of the boundary where the tangential magnetic field is specified ($\partial\Gamma_2$)

$$\hat{n} \times \nabla \times \bar{A} = \mu\hat{n} \times \bar{H} \tag{11.121}$$

$$\hat{n} \cdot \varepsilon\bar{A} = -\frac{1}{\omega^2}\nabla^{\tan} \cdot (\hat{n} \times \bar{H}) \tag{11.122}$$

$$\frac{\partial\Phi}{\partial n} = 0 \tag{11.123}$$

where $\nabla^{\tan} \cdot \bar{V}$ denotes the surface divergence.

The preceding development constitutes one in which the primary unknowns are continuous quantities and thus should be applicable to the use of traditional scalar Lagrangian basis functions. The principal drawback to this approach appears to be the need to use four unknowns per node and the need to differentiate the potential functions in order to construct the fields. The literature provides more details about this formulation, as well as others in which vector and scalar potentials are the primary unknowns [45–48].

11.12 SUMMARY

This chapter has explored three-dimensional formulations for electromagnetic scattering. Different ways of truncating the computational domain for open regions have been emphasized, and a number of RBCs were described. Some are exact prior to discretization,

while others are approximate. If high accuracy is desired, it appears that a reasonably efficient formulation can be obtained by using an integral equation RBC in conjunction with an axisymmetric radiation boundary. This chapter has also illustrated the use of curl-conforming vector basis functions to discretize the curl–curl form of the three-dimensional vector Helmholtz equation. An alternative formulation permitting the use of traditional scalar Lagrangian basis functions was briefly summarized. Three-dimensional formulations require substantially more computer resources than two-dimensional approaches and are far from mature at the present time. It is likely that the next decade will see significant advances in these techniques.

REFERENCES

[1] J. S. Savage and A. F. Peterson, "Higher-order vector finite elements for tetrahedral cells," *IEEE Trans. Microwave Theory Tech.*, vol. 44, pp. 874–879, June 1996.

[2] J. C. Nedelec, "Mixed finite elements in R3," *Numer. Math.*, vol. 35, pp. 315–341, 1980.

[3] O. C. Zienkiewicz and R. L. Taylor, *The Finite Element Method.* London: McGraw-Hill, 1988.

[4] Y. Li, S. Zhu, and F. A. Fernandez, "The efficient solution of large sparse nonsymmetric and complex eigensystems by subspace iteration," *IEEE Trans. Magnetics*, vol. MAG-30, pp. 3582–3585, Sept. 1994.

[5] R. F. Harrington, *Time-Harmonic Electromagnetic Fields*, New York: McGraw-Hill, 1961.

[6] J. A. Stratton, *Electromagnetic Theory*, New York: McGraw-Hill, 1941.

[7] W. V. T. Rusch, A. C. Ludwig, and W. C. Wong, "Analytical techniques for quasi-optical antennas," in *The Handbook of Antenna Design*, eds. A. W. Rudge, K. Milne, A. D. Olver, and P. Knight, London, Peregrinus, 1986, pp. 101–109.

[8] J. Jin, *The Finite Element Method in Electromagnetics*, New York: Wiley, 1993.

[9] X. Yuan, "Three-dimensional electromagnetic scattering from inhomogeneous objects by the hybrid moment and finite element method," *IEEE Trans. Antennas Propagat.*, vol. 38, pp. 1053–1058, Aug., 1990.

[10] J.-M. Jin and J. L. Volakis, "Electromagnetic scattering by and transmission through a three-dimensional slot in a thick conducting plane," *IEEE Trans. Antennas Propagat.*, vol. 39, pp. 543–550, Apr. 1991.

[11] J.-M. Jin and J. L. Volakis, "A hybrid finite element method for scattering and radiation by microstrip patch antennas and arrays residing in a cavity," *IEEE Trans. Antennas Propagat.*, vol. 39, pp. 1598–1604, Nov. 1991.

[12] J. L. Volakis, A. Chatterjee, and L. C. Kempel, "Review of the finite element method for three-dimensional electromagnetic scattering," *J. Opt. Soc. Am. A*, vol. 11, pp. 1422–1433, Apr. 1994.

[13] G. E. Antilla and N. G. Alexopoulos, "Scattering from complex three-dimensional geometries by a curvilinear hybrid finite-element–integral-equation approach," *J. Opt. Soc. Am. A*, vol. 11, pp. 1445–1457, Apr. 1994.

[14] E. W. Lucas and T. P. Fontana, "A 3-D hybrid finite element/boundary element method for the unified radiation and scattering analysis of general infinite periodic arrays," *IEEE Trans. Antennas Propagat.*, vol. 43, pp. 145–153, Feb. 1995.

[15] W. E. Boyse and A. A. Seidl, "A hybrid finite element method for near bodies of revolution," *IEEE Trans. Magnet.*, vol. 27, pp. 3833–3836, Sept. 1991.

[16] W. E. Boyse and A. A. Seidl, "A hybrid finite element method for 3-D scattering using nodal and edge elements," *IEEE Trans. Antennas Propagat.*, vol. 42, pp. 1436–1442, Oct. 1994.

[17] T. Cwik, V. Jamnejad, and C. Zuffada, "Coupling finite element and integral equation representations to efficiently model large three-dimensional scattering objects," *Digest of the 1993 IEEE Antennas and Propagation Society International Symposium*, Ann Arbor, MI, pp. 1756–1759, June 1993.

[18] T. Cwik, V. Jamnejad, and C. Zuffada, "A comparison of partitioned and non-partitioned matrix solutions to coupled finite element-integral equations," *Abstracts of the 1993 URSI Radio Science Meeting*, Ann Arbor, MI, p. 253, June 1993.

[19] T. Cwik, C. Zuffada, and V. Jamnejad, "The coupling of finite element and integral equation representations for efficient three-dimensional modeling of electromagnetic scattering and radiation," in *Finite Element Software for Microwave Engineering*, eds. T. Itoh, G. Pelosi, and P. P. Silvester, New York: Wiley, 1996, pp. 147–167.

[20] C. H. Wilcox, "An expansion theorem for electromagnetic fields," *Comm. Pure Appl. Math.*, vol. 9, pp. 115–134, 1956.

[21] A. F. Peterson, "Absorbing boundary conditions for the vector wave equation," *Microwave Opt. Technol. Lett.*, vol. 1, pp. 62–64, Apr. 1988.

[22] A. F. Peterson, "Accuracy of 3D radiation boundary conditions for use with the vector Helmholtz equation," *IEEE Trans. Antennas Propagat.*, vol. 40, pp. 351–355, Mar. 1992.

[23] J. P. Webb and V. N. Kanellopoulos, "Absorbing boundary conditions for the finite element solution of the vector wave equation," *Microwave Opt. Technol. Lett.*, vol. 2, pp. 370–372, Oct. 1989.

[24] V. N. Kanellopoulos and J. P. Webb, "The importance of the surface divergence term in the finite element-vector absorbing boundary condition method," *IEEE Trans. Microwave Theory Tech.*, vol. 43, pp. 2168–2170, Sept. 1995.

[25] J. S. Savage, "Vector finite elements for the solution of Maxwell's equations." Ph.D. dissertation, Georgia Institute of Technology, Atlanta, 1997.

[26] S. P. Castillo and A. F. Peterson, "Solution of the 3-D vector wave equation in an open region using the finite element method," *Abstracts of the 1989 URSI Radio Science Meeting*, San Jose, CA, p. 328, June 1989.

[27] J. P. Webb and V. N. Kanellopoulos, "A numerical study of vector absorbing boundary conditions for the finite element solution of Maxwell's equations," *IEEE Microwave Guided Wave Lett.*, vol. 1, pp. 325–327, Nov. 1991.

[28] A. Chatterjee, J. M. Jin, and J. L. Volakis, "Edge-based finite elements and vector ABC's applied to 3-D scattering," *IEEE Trans. Antennas Propagat.*, vol. 41, pp. 221–226, Feb. 1993.

[29] J. D'Angelo and I. D. Mayergoyz, "Finite element methods for the solution of RF radiation and scattering problems," *Electromagnetics*, vol. 10, pp. 177–199, 1990.

[30] J. D'Angelo and I. D. Mayergoyz, "Three-dimensional RF scattering by the finite element method," *IEEE Trans. Magnet.*, vol. 27, pp. 3827–3832, Sept. 1991.

[31] W. Sun and C. A. Balanis, "Vector one-way wave absorbing boundary conditions for FEM applications," *IEEE Trans. Antennas Propagat.*, vol. 42, pp. 872–878, June 1994.

[32] B. Stupfel, "Absorbing boundary conditions on arbitrary boundaries for the scalar and vector wave equations," *IEEE Trans. Antennas Propagat.*, vol. 42, pp. 773–780, June 1994.

[33] A. Chatterjee and J. L. Volakis, "Conformal absorbing boundary conditions for the vector wave equation," *Microwave Opt. Technol. Lett.*, vol. 6, pp. 886–889, Dec. 1993.

[34] A. Chatterjee and J. L. Volakis, "Conformal absorbing boundary conditions for 3-D problems: Derivation and applications," *IEEE Trans. Antennas Propagat.*, vol. 43, pp. 860–866, Aug. 1995.

[35] J. M. Jin, J. L. Volakis, and V. V. Liepa, "Fictitious absorber for truncating finite element meshes in scattering," *IEE Proc. H*, vol. 139, pp. 472–476, Oct. 1992.

[36] J.-P. Berenger, "A perfectly matched layer for the absorption of electromagnetic waves," *J. Computat. Phys.*, vol. 114, pp. 185–200, 1994.

[37] D. S. Katz, E. T. Thiele, and A. Taflove, "Validation and extension to three dimensions of the Berenger PML absorbing boundary condition for FD-TD meshes," *IEEE Microwave Guided Wave Lett.*, vol. 4, pp. 268–271, 1994.

[38] Z. S. Sacks, D. M. Kingsland, R. Lee, and J.-F. Lee, "A perfectly matched anisotropic absorber for use as an absorbing boundary condition," *IEEE Trans. Antennas Propagat.*, vol. 43, pp. 1460–1463, Dec. 1995.

[39] D. M. Kingsland, J. Gong, J. L. Volakis, and J.-F. Lee, "Performance of an anisotropic artificial absorber for truncating finite element meshes," *IEEE Trans. Antennas Propagat.*, vol. 44, pp. 975–981, July 1996.

[40] M. A. Morgan, S. -K. Chang, and K. K. Mei, "Coupled azimuthal potentials for electromagnetic field problems in inhomogeneous axially symmetric media," *IEEE Trans. Antennas Propagat.*, vol. 25, pp. 413–417, May 1977.

[41] R. K. Gordon and R. Mittra, "PDE techniques for solving the problem of radar scattering by a body of revolution," *Proc. IEEE*, vol. 79, pp. 1449–1458, Oct. 1991.

[42] D. J. Hoppe, L. W. Epp, and J.-F. Lee, "A hybrid symmetric FEM/MOM formulation applied to scattering by inhomogeneous bodies of revolution," *IEEE Trans. Antennas Propagat.*, vol. 42, pp. 798–805, June 1994.

[43] A. Khebir, J. D'Angelo, and J. Joseph, "A new finite element formulation for RF scattering by complex bodies of revolution," *IEEE Trans. Antennas Propagat.*, vol. 41, pp. 534–541, May 1993.

[44] J.-F. Lee, G. M. Wilkins, and R. Mittra, "Finite element analysis of axisymmetric cavity resonator using a hybrid edge element technique," *IEEE Trans. Microwave Theory Tech.*, vol. 41, pp. 1981–1987, Nov. 1993.

[45] J. R. Brauer, ed., *What Every Engineer Should Know about Finite Element Analysis*, New York: Marcel Dekker, 1993.

[46] W. E. Boyse, D. R. Lynch, K. D. Paulsen, and G. N. Minerbo, "Continuous potential Maxwell's equation solution on nodal-based finite elements," *IEEE Trans. Antennas Propagat.*, vol. 40, pp. 1192–1200, 1992.

[47] K. D. Paulsen, W. E. Boyse, and D. R. Lynch, "Nodal based finite element modeling of Maxwell's equations," *IEEE Trans. Antennas Propagat.*, vol. 40, pp. 642–651, June 1992.

[48] K. D. Paulsen, "Finite element solution of Maxwell's equations with Helmholtz forms," *J. Opt. Soc. Am. A*, vol. 11, pp. 1434–1444, Apr. 1994.

PROBLEMS

P11.1 Describe the appropriate boundary conditions to be imposed on the surface of a perfect magnetic conductor, and discuss their implementation in connection with the weak differential equations in (11.6) and (11.7).

P11.2 Evaluate (11.35) and (11.36) for the possible combinations of coordinates associated with element matrix entries for the LT/QN basis and testing functions.

P11.3 Consider an infinite structured mesh obtained by dividing a regular cubical-cell mesh into tetrahedrons, with five tetrahedrons per cube. Determine the number of CT/LN basis functions per cell and the number of LT/QN basis functions per cell associated with this type of mesh. In addition, determine the average number of nonzero matrix entries per unknown for both basis function types. Using the average number of nodes per cell, compare these numbers with similar estimates for linear and quadratic Lagrangian basis functions, assuming that three Lagrangian functions per node are used to represent the same three-dimensional field.

P11.4 By expanding a uniform plane-wave incident field in terms of spherical harmonics, rewrite the RBC in (11.47) in terms of the total electric field.

P11.5 The RBC in (11.47) involves a summation over the spherical eigenfunctions. Discuss the convergence of this summation as a function of the index n.

P11.6 Using the integral formulas

$$\int_0^\pi \left[\frac{\partial P_n^m(\cos\theta)}{\partial\theta} \frac{\partial P_q^m(\cos\theta)}{\partial\theta} + \frac{m^2 P_n^m(\cos\theta) P_q^m(\cos\theta)}{\sin^2\theta} \right] \sin\theta \, d\theta = 0 \qquad q \neq n$$

$$\int_0^\pi \left[\left(\frac{\partial P_n^m(\cos\theta)}{\partial\theta} \right)^2 + \left(\frac{m P_n^m(\cos\theta)}{\sin\theta} \right)^2 \right] \sin\theta \, d\theta = \frac{2n(n+1)}{2n+1} \frac{(n+|m|)!}{(n-|m|)!}$$

verify the following orthogonality conditions involving the spherical vector wave functions in (11.38) and (11.39):

$$\bar{M}_{mn} \cdot \bar{N}_{mn} = 0$$

$$\int_0^{2\pi} \int_0^\pi \bar{M}_{mn} \cdot \bar{M}_{pq} \sin\theta \, d\theta \, d\phi = \begin{cases} \beta_{mn} & p = -m, q = n \\ 0 & \text{otherwise} \end{cases}$$

$$\int_0^{2\pi} \int_0^\pi \bar{N}_{mn}^{\tan} \cdot \bar{N}_{pq}^{\tan} \sin\theta \, d\theta \, d\phi = \begin{cases} \gamma_{mn} & p = -m, q = n \\ 0 & \text{otherwise} \end{cases}$$

where "tan" refers to the theta and phi components only,

$$\beta_{mn} = \left(\frac{\hat{H}_n^{(2)}(kr)}{r} \right)^2 \frac{4\pi n(n+1)}{2n+1} \frac{(n+|m|)!}{(n-|m|)!}$$

$$\gamma_{mn} = \left(\frac{\hat{H}_n^{(2)\prime}(kr)}{r} \right)^2 \frac{4\pi n(n+1)}{2n+1} \frac{(n+|m|)!}{(n-|m|)!}$$

Using these orthogonality conditions, derive an alternate form of the spherical eigenfunction RBC, leaving the result in terms of the scattered field.

P11.7 Derive an expression for the scattering cross section as a function of the coefficients of the spherical vector wave functions in (11.38) and (11.39).

P11.8 Using the vector basis function definitions (Chapter 9), demonstrate the equivalence of a CT/LN representation of the magnetic field $\bar{H}$ throughout tetrahedral cells and a CN/LT representation of the equivalent surface current $\bar{J}_s$ on the triangular faces of the same cells.

P11.9 Develop a discretization of (11.52) for the MFIE part ($\alpha = 0$) of the equation using CN/LT basis functions defined on triangular patches and razor-blade testing functions (Section 10.2). Provide explicit entries for the system in (11.53). *Hint:* These entries are similar to those given in Chapter 10.

P11.10 Generalize the outward-looking formulation embodied in Equation (11.62) for the situation when the basis functions used within the interior region Γ are not the same as the basis functions used to represent the equivalent surface current densities $\bar{J}_s$ and $\bar{K}_s$ within the integral equation RBC. In this case, the coefficients of the interior expansion are not directly related to either of those on the surface, and one cannot assume that $\mathbf{e}^{\text{bound}} = \mathbf{k}$. Develop a way of defining one set of coefficients in terms of the other; that is, describe the linear operator f associated with the relation $\mathbf{e}^{\text{bound}} = f(\mathbf{k})$.

P11.11 For body-of-revolution integral equation formulations (Chapter 8), the number of important cylindrical harmonics associated with a normally incident wave is sometimes estimated as $2(6 + k\rho)$, where ρ is the largest radius of the boundary. How many harmonics must be included for a right-circular cylindrical region of radius (a) 1λ, (b) 10λ, and (c) 50λ?

P11.12 Consider a heterogeneous region contained within a right- circular cylindrical boundary having outside length 10λ and radius 3λ, where λ is the free-space wavelength.

(a) Compare the volume of the cylindrical region to that of a sphere of radius 5.9λ (roughly the smallest sphere that encloses the cylinder).

(b) Estimate the number of exterior unknowns needed to pad the tetrahedral-cell computational domain from the cylinder out to a sphere of radius 5.9λ, assuming that CT/LN basis functions are used and that the longest cell edge may not exceed 0.1λ. If the number of unknowns arising within the cylindrical region is 1.5 million, what percentage of the total number of unknowns is used to pad to the spherical boundary?

(c) Repeat part (b) under the assumption that a conformable RBC is imposed on a slightly larger right-circular cylinder whose boundary is a distance of 0.3λ outside the original cylinder.

P11.13 The local RBC in (11.74) can be obtained by equating the left-hand side of (11.73) with zero and using the Helmholtz equation to eliminate the term involving the $\hat{r} \times \nabla \times (\hat{r} \times \nabla \times \bar{E}^s)$ operator. Verify this derivation to obtain (11.74).

P11.14 The spherical vector wave functions $\bar{M}_{mn}$ in (11.38) and $\bar{N}_{mn}$ in (11.39) are associated with the TE-to-r and TM-to-r parts of the scattered electric field, respectively. By applying the differential operators in (11.79)–(11.81) to these functions, verify that the operator in (11.79) only recovers the TE-to-r part of the field while those in (11.80) and (11.81) only recover the TM-to-r part.

P11.15 Using the spherical vector wave functions $\bar{M}_{mn}$ and $\bar{N}_{mn}$ in (11.38) and (11.39), obtain an expression for the error in the second-order local RBCs in (11.74) and (11.77) when applied to the mnth harmonic. (Develop separate expressions for the error in the TE-to-r part of the field and the TM-to-r part of the field.)

P11.16 Study the various differential operators comprising the RBCs in (11.87), (11.88), and (11.89), and try to assess the differences between them. Under what conditions do

they become equivalent? (For example, what happens as $r \to \infty$? What happens if $\nabla \cdot \bar{E}^s_{\tan} = 0$?)

P11.17 Show that the conformable RBCs defined by the coefficients in (11.92) and (11.93) and (11.94)–(11.97) reduce to the spherical-boundary RBC in (11.77) if $\kappa_1 = \kappa_2 = 1/r$.

P11.18 Discuss the computation of the scattering cross section, assuming that the vector Helmholtz equation coupled with a local RBC is used to determine the electric field associated with a three-dimensional scatterer. What different approaches are possible? What approximations are involved in each case? Recommend an approach.

P11.19 Suppose a lossy isotropic homogeneous region bounded by a perfect conductor is used to terminate the computational domain in a scattering problem. (In other words, a scatterer surrounded by a region of free space is enclosed within a lossy layer bounded by a perfect conductor.) Assuming that the material has a loss tangent of 1% and has a locally planar surface, how thick must the region be to reduce the reflections from the perfect conductor backing to a level less than that from the interface between the free-space region adjacent to the scatterer and the lossy absorber? Estimate the level of reflection likely from this interface, and comment on the number of additional unknowns required to represent the field throughout this region.

P11.20 (a) Show that a uniform plane wave of the form

$$\bar{E} = \hat{y} E_0 e^{-j\beta_x x} e^{-j\beta_z z}$$

is a valid solution to Maxwell's equations in a medium with relative permittivity and permeability tensors of the form

$$\bar{\bar{\varepsilon}}_r = \begin{bmatrix} a & 0 & 0 \\ 0 & a & 0 \\ 0 & 0 & b \end{bmatrix} \qquad \bar{\bar{\mu}}_r = \begin{bmatrix} c & 0 & 0 \\ 0 & c & 0 \\ 0 & 0 & d \end{bmatrix}$$

provided that

$$\frac{\beta_x^2}{d} + \frac{\beta_z^2}{c} = \omega^2 \mu_0 \varepsilon_0 a$$

Repeat your calculations for a wave of the form

$$\bar{H} = \hat{y} H_0 e^{-j\beta_x x} e^{-j\beta_z z}$$

to show that the phase constants must satisfy

$$\frac{\beta_x^2}{b} + \frac{\beta_z^2}{a} = \omega^2 \mu_0 \varepsilon_0 c$$

(b) Consider a wave incident at an arbitrary angle from free space into a medium with the above permittivity and permeability tensors. Show that the reflection coefficient associated with the perpendicular polarized wave in (11.99) is

$$\Gamma_\perp = \frac{\cos\theta/\eta - \beta_z/\omega\mu_0 c}{\cos\theta/\eta + \beta_z/\omega\mu_0 c}$$

while the reflection coefficient for the parallel polarized wave in (11.100) is

$$\Gamma_\parallel = \frac{\eta\cos\theta - \beta_z/\omega\varepsilon_0 a}{\eta\cos\theta + \beta_z/\omega\varepsilon_0 a}$$

Find conditions on a, b, c, and d that simultaneously eliminate reflections for both polarizations.

P11.21 Develop weak differential equations for the potential function formulation embodied in (11.116) and (11.117), and discuss the implementation of the associated boundary conditions in (11.118)–(11.123).